DTU Library

Topology optimization of compliant mechanisms considering stress constraints, manufacturing uncertainty and geometric nonlinearity

Assis da Silva, Gustavo; Beck, André Teófilo; Sigmund, Ole

Published in:
Computer Methods in Applied Mechanics and Engineering

Link to article, DOI:
10.1016/j.cma.2020.112972

Publication date:
2020

Document Version
Peer reviewed version

Topology optimization of compliant mechanisms considering stress constraints, manufacturing uncertainty and geometric nonlinearity

Gustavo Assis da Silva[a], André Teófilo Beck[a], Ole Sigmund[b]

[a]Department of Structural Engineering, São Carlos School of Engineering, University of São Paulo, 13.566-590, São Carlos, SP, Brazil
[b]Department of Mechanical Engineering, Solid Mechanics, Technical University of Denmark, Nils Koppels Alle, B. 404, 2800 Kgs. Lyngby, Denmark

Abstract

This paper proposes and investigates two formulations to topology optimization of compliant mechanisms considering stress constraints, manufacturing uncertainty and geometric nonlinearity. The first formulation extends the maximum output displacement robust approach with stress constraints to incorporate the effects of geometric nonlinear behavior during the optimization process. The second formulation relies on the concept of path-generating mechanisms, where not only the final configuration is important, but also the load-displacement equilibrium path. A novel path-generating formulation is thus proposed, not only to achieve the prescribed equilibrium path, but also to take stress constraints and manufacturing uncertainty into account during the optimization process. Although both formulations have different goals, the same main techniques are employed: density approach to topology optimization, augmented Lagrangian method to handle the large number of stress constraints, three-field robust approach to handle the manufacturing uncertainty, and the energy interpolation scheme to handle convergence issues due to large deformation in void regions. Several numerical examples are addressed to demonstrate applicability of the proposed approaches. The optimized results are post-processed with body-fitted finite element meshes. Obtained results demonstrate that: (1) the proposed nonlinear analysis based maximum output displacement approach is able to provide solutions with good performance in situations of large displacements, with stress and manufacturing requirements satisfied; (2) the linear analysis based maximum output displacement approach provides optimized topologies that show large stress constraint violations and rapidly varying stress behavior under uniform boundary variation, when these are post-processed with full nonlinear analysis; (3) the proposed path-generating formulation is able to provide solutions that follow the prescribed control points, including stress robustness.

Keywords: Topology optimization, Robust design, Compliant mechanisms, Manufacturing uncertainty, Stress constraints, Geometric nonlinearity

1. Introduction

Topology optimization is an important tool employed in the design of high performance structures [1, 2]. One important application is the design of compliant mechanisms [3]. This paper proposes and investigates two formulations to topology design of compliant mechanisms subjected to: (1) geometric nonlinearity; (2) stress constraints; and (3) manufacturing uncertainty.

It is acknowledged in the literature, that each of these three topics is a challenge by itself. The consideration of geometric nonlinear behavior in topology optimization, for instance, introduces serious convergence issues in the

Email addresses: gustavoas@usp.br (Gustavo Assis da Silva), atbeck@sc.usp.br (André Teófilo Beck), sigmund@mek.dtu.dk (Ole Sigmund)

problem when fictitious domain approaches are employed, in which void regions are modeled as solid material with very low stiffness [4]. These convergence issues are due to excessive distortion of elements in regions under very large deformation, as related by several works on finite strain topology design [4–13]. Even if the solid phase of the optimized topology contains regions of small strain only, the void phase may contain regions of large strain, in order to accommodate the large displacements of the solid phase [4]. In order to handle these convergence issues, some techniques were proposed in the past: relaxation of the convergence criterion for the equilibrium iterations [5], the element removal and reintroduction strategy [7], the element connectivity parameterization [8], the additive hyperelasticity technique [11], and the energy interpolation scheme [4]; to name a few. Some authors show that use of nonlinear material models, instead of the traditional Saint Venant–Kirchhoff model, also helps at alleviating the convergence issues during the equilibrium iterations [9, 14], although it is not completely effective to handle regions under very large deformation [4].

The other two topics also present several challenges, and are still subject to intensive research in the literature. Since the pioneering work of Duysinx and Bendsøe [15], researchers have proposed several techniques to address stress constraints in continuum topology optimization (see, e.g., [16–30]). Among these works, there are some recent papers that specifically address the compliant mechanism design problem [26–30]. The main challenges associated with the stress failure criterion in continuum topology optimization are the singularity phenomenon and the large number of local stress constraints [15]. Among the several techniques proposed to alleviate these difficulties, we have the stress constraint relaxation techniques [15, 31, 32], to handle the singularity phenomenon, and the aggregation approaches [17, 21, 33], to handle the large number of stress constraints, as the most popular ones. Recent papers on stress-based topology optimization also address the problem under the effect of geometric nonlinearity [10], and manufacturing uncertainty [34, 35]; however, to the authors' best knowledge, the simultaneous consideration of stress constraints, geometric nonlinearity and manufacturing uncertainty has not been addressed before.

In order to address manufacturing uncertainty in continuum topology design, Sigmund [36] and Wang et al. [37] proposed the three-field density projection approach, where eroded and dilated density fields are employed together with the actual (intermediate) topology, to simulate extreme uniform manufacturing errors during the optimization process. Since then, several techniques were proposed to handle manufacturing uncertainty in topology optimization [38–48], including some papers addressing the topology design problem considering both the manufacturing uncertainty and geometric nonlinear behavior [41, 46, 48]; however, without the stress considerations.

This paper proposes two formulations to address the topology design of compliant mechanisms subjected to geometric nonlinearity, stress constraints, and manufacturing uncertainty. The first one extends the formulation proposed by Da Silva et al. [35], which addresses the maximum output displacement stress-constrained compliant mechanism design problem considering infinitesimal strain theory, in order to include the geometric nonlinear behavior. The second one is a novel path-generating approach, based on the work by Pedersen et al. [6], to handle the path-generating problem, but also considering the stress constraints and uniform manufacturing error robustness. With this study, we intend to take a further step towards the topology design of compliant mechanisms that satisfy realistic engineering requirements, through the simultaneous consideration of geometric nonlinearity, stress failure criterion, and manufacturing uncertainty in the formulation.

The paper is organized as follows: the proposed maximum output displacement and path-generating formulations are presented in section 2; the finite strain theory is addressed in section 3; the proposed stress interpolation scheme is shown in section 4; optimization strategy is shown in section 5; optimization examples and proper validation are shown in section 6; and concluding remarks are given in section 7. Details on the sensitivity analyses are given in the appendix.

2. Proposed formulations

Topology optimization of compliant mechanisms is addressed by distribution of isotropic material in a fixed design domain. The traditional density approach to topology optimization [2] is employed: the design domain is discretized with the finite element method [49], and each element of the mesh is associated with a relative density varying from 0 (which represents void) to 1 (which represents solid). The optimization problems are formulated to simultaneously address the effect of stress constraints, uniform manufacturing error and geometric nonlinearity in the topology design of compliant mechanisms. The proposed formulations are based on the three-field robust approach presented in [37], which considers three fields of relative densities: eroded, intermediate and dilated. In this formulation, the intermediate topology is the robust design at the end of the optimization procedure, whereas eroded and dilated designs represent extreme manufacturing errors; the eroded being thinner, and the dilated being thicker than the intermediate one. The eroded and dilated designs capture the variability on the boundary of the topology that may occur due to manufacturing error, with the underlying assumption that the entire boundary is eroded or dilated by the same amount. Two formulations are proposed:

1. **Maximum output displacement formulation.** The main goal is the design of compliant mechanisms with extreme output displacements, while still satisfying the stress and manufacturing requirements. In this case, the physical densities are given by $\overline{\boldsymbol{\rho}}^{(e)}$, $\overline{\boldsymbol{\rho}}^{(i)}$ and $\overline{\boldsymbol{\rho}}^{(d)}$; associated with eroded, intermediate and dilated designs, respectively; these are associated with design variables $\boldsymbol{\rho}$ through a density filter with threshold projection, as described in subsection 2.1.

2. **Path-generating formulation.** The main goal is the design of compliant mechanisms that pass through specific control points given by the designer, also considering both the stress and manufacturing requirements. The physical densities are given by $\overline{\overline{\boldsymbol{\rho}}}^{(e)}$, $\overline{\overline{\boldsymbol{\rho}}}^{(i)}$ and $\overline{\overline{\boldsymbol{\rho}}}^{(d)}$; these are obtained by means of the double filter approach, as described in subsection 2.2. Use of double filter instead of standard filter proved necessary to alleviate large gray regions, which result from use of the error function alone in this formulation, as demonstrated in subsection 6.2. In general, simple filter operations require an active volume constraint to work well.

The resulting problems, in discretized form, are solved with use of a gradient-based algorithm, as discussed in section 5. Both formulations are motivated and presented in detail in the next subsections.

2.1. Proposed maximum output displacement formulation

The maximum output displacement compliant mechanism design problem considering stress constraints is addressed in [35], as an extension of the standard min-max approach developed in [37]; however, the formulation proposed in [35] was developed to handle linear elastic problems only. In this paper, we generalize the stress-constrained formulation presented in [35], in order to allow the design of large displacement compliant mechanisms considering both stress constraints and manufacturing uncertainty. The proposed generalization, considering the von Mises failure criterion, is given by

$$
\begin{aligned}
\underset{\boldsymbol{\rho}}{\text{Min.}} \quad & \frac{k_{in}}{f_{in}} \max\left(u_{out}\left(\overline{\boldsymbol{\rho}}^{(e)}\right), u_{out}\left(\overline{\boldsymbol{\rho}}^{(i)}\right), u_{out}\left(\overline{\boldsymbol{\rho}}^{(d)}\right)\right) + k_v V_f\left(\overline{\boldsymbol{\rho}}^{(d)}\right) \\
\text{s. t.} \quad & V_f\left(\overline{\boldsymbol{\rho}}^{(d)}\right) \leqslant V_{up}^{(d)} \\
& V_f\left(\overline{\boldsymbol{\rho}}^{(d)}\right) \geqslant V_{low}^{(d)} \\
& \frac{\sigma_{eq}^{(k)}\left(\overline{\boldsymbol{\rho}}^{(j)}\right)}{\sigma_y} - 1 \leqslant 0 && j \in \{e, i, d\} \text{ and } k = 1, 2, ..., N_k \\
& \delta\Pi\left(\overline{\boldsymbol{\rho}}^{(j)}\right) = 0 && j \in \{e, i, d\} \\
& 0 \leqslant \rho_e \leqslant 1 && e = 1, 2, ..., N_e
\end{aligned}
\quad , \qquad (1)
$$

where the equilibrium configuration is represented through stationarity of the systems total potential energy $\Pi\left(\overline{\boldsymbol{\rho}}^{(j)}\right)$, as $\delta\Pi\left(\overline{\boldsymbol{\rho}}^{(j)}\right) = 0$, for $j \in \{e, i, d\}$. The proposed generalization allows use of any specific strain energy function to represent the stored energy in an elastic material. A hyperelastic material model based on the Green strain tensor $\mathbf{E}$, for instance, instead of the standard linear elastic model based on the infinitesimal strain tensor $\boldsymbol{\varepsilon}$, may be employed. This allows use of the finite strain theory in the formulation and, hence, the design of large displacement compliant mechanisms.

In Equation (1), f_{in}/k_{in} is the free displacement of the input actuator, which depends on both the input load f_{in} and input stiffness k_{in}, employed here for the purpose of normalization; $u_{out}\left(\overline{\boldsymbol{\rho}}^{(j)}\right) = \boldsymbol{\Lambda}_{out}^{T}\mathbf{U}\left(\overline{\boldsymbol{\rho}}^{(j)}\right)$, for $j \in \{e, i, d\}$, is the output displacement of the compliant mechanism, which depends on the localization vector $\boldsymbol{\Lambda}_{out}$, which takes either 1 or -1 at the degree of freedom that corresponds to the output degree of freedom and zero otherwise; k_v is a weighting parameter defined by the designer (chosen as $k_v = 2$ in this paper, based on the hints by [35]), employed here to alleviate the spurious solid regions that may appear on the optimized topologies when the upper volume constraint is not active (see [35] for details); $V_f\left(\overline{\boldsymbol{\rho}}^{(d)}\right) = \frac{V\left(\overline{\boldsymbol{\rho}}^{(d)}\right)}{V_{domain}}$ is the volume fraction of the dilated design; $V\left(\overline{\boldsymbol{\rho}}^{(d)}\right) = \sum_{e=1}^{N_e} V_e \overline{\rho}_e^{(d)}$ is the structural volume of the dilated topology; V_e is the volume of element e; V_{domain} is the volume of the design domain; $V_{up}^{(d)}$ and $V_{low}^{(d)}$ are upper and lower volume fractions for the dilated design, respectively; $\sigma_{eq}^{(k)}\left(\overline{\boldsymbol{\rho}}^{(j)}\right)$ is the von Mises equivalent stress computed at point k, for $j \in \{e, i, d\}$; σ_y is the yield stress; N_k is the number of points of stress computation; ρ_e is the design variable associated with element e; and N_e is the number of elements in the finite element mesh.

2.1.1. *Density filter with threshold projection*

In the proposed formulation, we employ the three-field density approach as presented in [37], which makes use of one set of design variables, $\boldsymbol{\rho}$, one set of filtered densities, $\tilde{\boldsymbol{\rho}}$, and three sets of relative densities: $\overline{\boldsymbol{\rho}}^{(e)}$, $\overline{\boldsymbol{\rho}}^{(i)}$ and $\overline{\boldsymbol{\rho}}^{(d)}$; associated with eroded, intermediate and dilated designs, respectively, that are the actual physical densities.

Relative densities are related to design variables through a density filter with threshold projection [37]. The relative density of element e, $\overline{\rho}_e$, is computed as

$$\overline{\rho}_e = \frac{\tanh(\beta\eta) + \tanh(\beta(\tilde{\rho}_e - \eta))}{\tanh(\beta\eta) + \tanh(\beta(1-\eta))}, \tag{2}$$

where $\tilde{\rho}_e$ is the filtered relative density of element e, obtained from a linear projection

$$\tilde{\rho}_e = \frac{\sum_{i\in\vartheta_e} w(\mathbf{x}_i) V_i \rho_i}{\sum_{i\in\vartheta_e} w(\mathbf{x}_i) V_i}, \tag{3}$$

over the design variables $\boldsymbol{\rho}$, in a circular neighborhood ϑ_e, centered in element e, which contains all the elements whose centers are within a radius R specified by the designer.

The linear weighting function is defined as

$$w(\mathbf{x}_i) = R - \|\mathbf{x}_i - \mathbf{x}_e\|, \tag{4}$$

where $\mathbf{x}_i$ are the coordinates of the center of element i and $\mathbf{x}_e$ are the coordinates of the center of the neighborhood ϑ_e.

In Equation (2), β controls the non-linearity and η the projection level of the smoothed Heaviside approximation. For $\beta \to 0$ we have a linear behavior between relative and filtered densities, whereas for $\beta \to \infty$ we have a Heaviside step function [37]. The parameter β is updated through a continuation strategy during the optimization procedure, starting from a small value $\beta^{(1)}$, up to a maximum value β_{max}. In this paper, the value of β_{max} is set based on the hints proposed in [34], in order to allow a thin smooth transition boundary of intermediate material between solid and void phases. Da Silva et al. [34] propose the choice of β_{max} based on the value of $\beta_{lim} = 2R/l_e$. It represents the upper bound to parameter β in order to ensure a smooth transition boundary of intermediate material, between solid and void phases, of length equal to the side of a square element, l_e. Use of $\beta_{max} \cong \beta_{lim}/2 = R/l_e$, for instance, allows a smooth transition boundary slightly thicker than l_e. Moreover, it is demonstrated that when this choice is associated with a reasonable choice of stress constraint relaxation function, stress accuracy at the boundaries of the structure is ensured. Although the numerical experiments shown in [34] are performed under the hypothesis of linear elasticity, we employ the same scheme to compute β_{max} in this paper, since the artificial stress concentration on jagged boundaries does not affect linear elastic problems only. Moreover, as presented later in the results section, good agreement is observed between pixel-based and interpreted body-fitted von Mises equivalent stresses. The continuation strategy employed in this paper to update the value of β during the optimization procedure is given in detail in [35].

The parameter $\eta \in [0, 1]$, in Equation (2), controls the amount of filtered densities $\tilde{\rho}_e$ projected to either 0 or 1, for $\beta \to \infty$. Each relative density field is associated with a distinct value of η, following the condition: $\eta_e > \eta_i > \eta_d$; where e, i, d refer to eroded, intermediate and dilated designs, respectively.

2.1.2. Stress constraint relaxation

In this paper, the plane stress hypothesis is considered. In this case, one can compute the von Mises equivalent stress at any point k as

$$\begin{aligned}\sigma_{eq}^{(k)}\left(\overline{\boldsymbol{\rho}}^{(j)}\right) &= f_\sigma\left(\overline{\rho}_k^{(j)}\right)\hat{\sigma}_{eq}^{(k)}\left(\overline{\boldsymbol{\rho}}^{(j)}\right) \\ &= f_\sigma\left(\overline{\rho}_k^{(j)}\right)\sqrt{\hat{\sigma}_{11(k)}^2\left(\overline{\boldsymbol{\rho}}^{(j)}\right) - \hat{\sigma}_{11(k)}\left(\overline{\boldsymbol{\rho}}^{(j)}\right)\hat{\sigma}_{22(k)}\left(\overline{\boldsymbol{\rho}}^{(j)}\right) + \hat{\sigma}_{22(k)}^2\left(\overline{\boldsymbol{\rho}}^{(j)}\right) + 3\hat{\sigma}_{12(k)}^2\left(\overline{\boldsymbol{\rho}}^{(j)}\right) + \sigma_{min}^2}\end{aligned} \tag{5}$$

where $f_\sigma\left(\overline{\rho}_k^{(j)}\right)$ is the stress interpolation function at point k, $\hat{\sigma}_{eq}^{(k)}\left(\overline{\boldsymbol{\rho}}^{(j)}\right)$ is the solid von Mises stress at point k, $\hat{\sigma}_{11(k)}$, $\hat{\sigma}_{22(k)}$ and $\hat{\sigma}_{12(k)}$ are the components of the solid Cauchy stress tensor at point k, and $\sigma_{min} = 1 \times 10^{-4}\sigma_y$ is a small value included in our implementations to ensure a positive number in the square root, thus avoiding numerical instabilities during the sensitivity analysis, needed for optimization with a gradient-based algorithm. In order to compute the components of the solid Cauchy stress tensor: $\hat{\sigma}_{11(k)}$, $\hat{\sigma}_{22(k)}$ and $\hat{\sigma}_{12(k)}$; we propose a stress interpolation scheme, Equation (29), shown in section 4, to be used with the energy interpolation scheme presented in subsection 3.1. The components of the solid stress tensor are computed considering the constitutive tensor of the base material [17]; however, they are not appropriate to be directly used in stress-constrained topology optimization, since the solid stresses may remain finite and larger than the yield stress when relative densities tend to zero, leading to the singularity phenomenon [15]. Stress constraint relaxation, in the form of a stress interpolation function in this paper, is thus necessary in order to avoid this issue and allow optimization with gradient-based algorithm.

The ε-relaxed approach [31, 33] is employed to relax the stress constraints, thus avoiding the singularity phenomenon, with $f_\sigma\left(\overline{\rho}_k^{(j)}\right) = \frac{\overline{\rho}_k^{(j)}}{\varepsilon\left(1-\overline{\rho}_k^{(j)}\right)+\overline{\rho}_k^{(j)}}$. As presented in [34], the proper choice of ε associated with a smooth transition boundary of proper thickness, between solid and void phases, can ensure stress accuracy and low stress oscillation after uniform boundary variation. When ε is too small, the stresses at the jagged edges of the structures are overestimated and strong stress oscillations may occur. On the other hand, when ε is too large, the stresses are underestimated. Following [34], we choose $\varepsilon = 0.2$, which is a reasonable choice when using $\beta_{max} \cong R/l_e$.

2.2. *Proposed path-generating formulation*

The path-generating formulation proposed in this paper is based on the work by Pedersen et al. [6], who proposed the minimization of an error function between prescribed and computed output displacements, in order to ensure that the resulting output point follows the prescribed control points for a given set of input loads. The main idea of the path-generating formulation is that not only the final configuration is important, but also the equilibrium path. The main novelty of the formulation proposed in this paper, Equation (6), with respect to the path-generating formulation proposed in Pedersen et al. [6], is the additional consideration of both stress constraints and manufacturing tolerance. The proposed path-generating formulation is given by

$$\begin{array}{lll}
\underset{\boldsymbol{\rho}}{\text{Min.}} & \left(\dfrac{k_{in}}{f_{in,M}}\right)^2 \displaystyle\sum_{j\in\{e,i,d\}} \sum_{m=1}^{M} \left(u_{out,m}\left(\overline{\overline{\boldsymbol{\rho}}}^{(j)}\right) - u^*_{out,m}\right)^2 & \\
 & & \\
\text{s. t.} & V_f\left(\overline{\overline{\boldsymbol{\rho}}}^{(d)}\right) \leqslant V_{up}^{(d)} & \\
 & \dfrac{\sigma_{eq}^{(k)}\left(\overline{\overline{\boldsymbol{\rho}}}^{(j)}\right)}{\sigma_y} - 1 \leqslant 0 & j \in \{e,i,d\} \text{ and } k = 1,2,...,N_k \\
 & \delta\Pi\left(\overline{\overline{\boldsymbol{\rho}}}^{(j)}\right) = 0 & j \in \{e,i,d\} \\
 & 0 \leqslant \rho_e \leqslant 1 & e = 1,2,...,N_e
\end{array}, \qquad (6)$$

where M is the number of control points prescribed by the designer; $u_{out,m}$ is the computed displacement at the output port for the m-th input load $f_{in,m}$; and $u^*_{out,m}$ is the m-th prescribed output displacement, which is also associated with $f_{in,m}$. The constant $\left(\frac{k_{in}}{f_{in,M}}\right)^2$ is employed here for the purpose of normalization, where $f_{in,M}$ is the largest input load in absolute value, associated with the final prescribed output displacement $u^*_{out,M}$. The stress constraints, $\frac{\sigma_{eq}^{(k)}\left(\overline{\overline{\boldsymbol{\rho}}}^{(j)}\right)}{\sigma_y} - 1 \leqslant 0$, are applied for the largest input load in absolute value, $f_{in,M}$.

Note that a min-max type formulation could be employed to address the path-generating problem as well: as the minimization of the maximum difference among all computed and prescribed displacements. However, we preferred to base our path-generating formulation on the original approach by Pedersen et al. [6], where the least squares fitting is employed. Moreover, although not implemented herein, use of a min-max formulation in this case would put too much weight on the largest displacement case and may ignore the smaller displacement cases.

While the maximum output displacement formulation, Equation (1), does not take the equilibrium path into account, the path-generating formulation, Equation (6), can be employed to control the equilibrium path, to a certain extent, depending on the control points given by the designer. Use of the path-generating formulation allows for example to control the shape of the $f_{in} \times u_{out}$ graph of the resulting mechanism.

Pedersen et al. [6] observed that use of the minimum error formulation alone, without any additional requirement to increase the ability of the mechanism to transfer force from the input point to the output point, may lead to topologies entirely comprised of intermediate material. To prevent this issue, they proposed use of a modified objective function, introducing the additional requirement that the resulting mechanism also has to pass through the control points when two separate counter load cases are applied at each control point. Pedersen et al. [6] demonstrated, through numerical experiments, that when such a requirement is included in the formulation, the resulting mechanism is stiffer and more black and white, with less regions of intermediate material.

During our numerical investigations with the path-generating formulation, we confirmed that use of the minimum error formulation alone may lead to topologies comprised of large regions of intermediate material. Moreover, we verified that use of the standard density filter with threshold projection in Equation (6) may not be sufficient to remove all grey areas of the resulting mechanism, as shown later in the results section. However, instead of including additional stiffness requirements as suggested by [6], we decided to employ the novel double filter technique proposed by Christiansen et al. [45], i.e., use of $\bar{\bar{\boldsymbol{\rho}}}$ to represent the actual physical densities, since this approach turns out to be a powerful tool to alleviate the numerical instabilities which arise from use of the error function alone in the formulation.

It should be emphasized that the grey regions, resulting from use of the error function alone in the path-generating formulation, have different cause from the spurious solid regions that may appear in the maximum output displacement formulation, when the upper volume fraction is not active. The main issue associated with spurious material in the path-generating formulation is that, as soon as the path is prescribed, there may be no need to use material the best possible way, regarding the ability to transfer force from the input to the output, making room for the appearance of gray regions [6]. On the other hand, the spurious material issue associated with the maximum output displacement formulation arises from the fact that the upper volume fraction is sometimes not active, due to the very small stress level employed, enforcing lower volume fractions to the structure and making room for the appearance of spurious material regions, mainly on the dilated topology, as described in [35]. In theory, both issues could be handled by the proper adjustment of an ideal upper volume fraction. However, the choice of a proper volume fraction varies from problem to problem, being impractical in most cases. In order to handle the spurious material issue in the maximum output displacement problem, Equation (1), we follow the hints by [35] and add the volume of the dilated topology in the objective function, resulting in topologies without grey regions, as shown in the results section. Use of this same strategy in the path-generating formulation, Equation (6), does not work properly, since the algorithm often prioritizes the volume minimization instead of the design of the path, making the choice of the weight of the dilated volume in the objective function a challenging and problem dependent task. Use of the double filter approach, thus, arises as an effective solution to alleviate these issues, associated with the path-generating problem. We observed that the extra regularization over the filtered density field helps the achievement of almost black and white topologies for relatively small values of β, in which eroded and dilated designs actually represent near-uniform boundary variations. For the cases we investigated using the double filter approach, there was no need to use additional volume nor stiffness considerations.

Although not implemented herein, we realize that the double filter approach could also be employed to address the maximum output displacement problem. However, we preferred to follow the approach by Da Silva et al. [35] and simply add the volume of the dilated structure in the objective function instead. As discussed in [35], when the volume of the dilated structure is included in the objective function, the optimizer sometimes prefers to minimize the volume instead of the displacements, leading to a void design. Since the stress constraints are relaxed, the void solution is accepted by the algorithm, since zero densities mean zero stresses, i.e., a feasible design in this case. The lower volume fraction limit, as considered in the maximum output displacement formulation, Equation (1), acts to preventing this situation. Note that since the volume is not considered as objective in the path-generating problem, Equation (6), the lower volume constraint is not necessary there. The investigation of the double filter approach in the maximum output displacement formulation is beyond the scope of this work.

2.2.1. Double filter approach

In the path-generating formulation, we employ the double filter approach as presented in [45], which makes use of one set of design variables, $\boldsymbol{\rho}$, one set of first level filtered densities, $\tilde{\boldsymbol{\rho}}$, one set of first level projected densities, $\overline{\boldsymbol{\rho}}$, one set of second level filtered densities, $\tilde{\overline{\boldsymbol{\rho}}}$, and three sets of second level projected densities: $\overline{\overline{\boldsymbol{\rho}}}^{(e)}$, $\overline{\overline{\boldsymbol{\rho}}}^{(i)}$ and $\overline{\overline{\boldsymbol{\rho}}}^{(d)}$; associated with eroded, intermediate and dilated designs, respectively, that are the actual physical densities.

The double filter approach is applied according to the following procedure:

1. Design variables $\boldsymbol{\rho}$ are filtered with Equation (3) for a filtering radius R_1, resulting in the first level filtered densities $\tilde{\boldsymbol{\rho}}$;

2. First level filtered densities $\tilde{\boldsymbol{\rho}}$ are projected with Equation (2) for β_1 and η_1, resulting in the first level projected densities $\overline{\boldsymbol{\rho}}$;
3. First level projected densities $\overline{\boldsymbol{\rho}}$ are filtered with Equation (3) for a filtering radius R_2, resulting in the second level filtered densities $\tilde{\overline{\boldsymbol{\rho}}}$;
4. Second level filtered densities $\tilde{\overline{\boldsymbol{\rho}}}$ are projected with Equation (2) for β_2 and three projection levels: η_e, η_i and η_d; resulting in the second level projected densities: $\overline{\overline{\boldsymbol{\rho}}}^{(e)}$, $\overline{\overline{\boldsymbol{\rho}}}^{(i)}$ and $\overline{\overline{\boldsymbol{\rho}}}^{(d)}$; respectively.

As discussed in [45], the double filter procedure introduces some additional parameters in the problem. In this paper, we choose $R_1 = 2R_2$, $\beta_1 = 2\beta_2$ and $\eta_1 = \eta_d$, based on the hints presented in [45]. Christiansen et al. [45] demonstrated, through numerical experiments, that the double filter approach can be used to limit variations of the filtered field $\tilde{\overline{\boldsymbol{\rho}}}$, ensuring near-uniform boundary variations for different projection levels, also in the cases where the standard robust approach may fail, as the acoustic cavity design problem addressed in their work.

3. Equilibrium analysis

This section presents some basics regarding the equilibrium analysis in the proposed formulation. Subsection 3.1 presents the energy interpolation scheme, employed to alleviate convergence issues associated with low density regions in finite strain topology optimization. Subsection 3.2 presents the employed specific strain energy function and some additional considerations regarding the plane stress hypothesis. Subsection 3.3 presents the positional numerical procedure, employed to find the equilibrium configuration of the structure.

Note that the physical densities are represented by $\overline{\boldsymbol{\rho}}$ in this section, although the same equations are used for the case where the double filter is employed, i.e., where the physical densities are represented by $\overline{\overline{\boldsymbol{\rho}}}$. In these cases, we simply replace $\overline{\boldsymbol{\rho}}$ with $\overline{\overline{\boldsymbol{\rho}}}$.

3.1. Energy interpolation scheme

It is acknowledged in the literature, that the convergence issues associated with low density regions under large deformation, in finite strain topology optimization, are very difficult to overcome and still being subject of intensive research [4, 11]. In this paper, we use the energy interpolation scheme, proposed by [4], in order to alleviate these convergence issues.

Wang et al. [4] demonstrated, through solution of the C-shaped numerical example from [8], that when a pure 0/1 topology is considered, there is no significant difference in the equilibrium configuration of the solid region, when modeling the void region with infinitesimal strain theory (linear analysis) or finite strain theory (nonlinear analysis). However, they verified that it is much easier to numerically find the equilibrium configuration when the void regions are modeled by using linear analysis, even though the void regions present very large deformations. In practical density-based topology optimization, however, we have to handle the intermediate densities, mainly at the first iterations of the optimization procedure, while the topology is forming; so that we cannot simply employ a crude interpolation scheme to model the solid regions with nonlinear analysis and the void regions with linear analysis. Wang et al. [4] thus proposed a smooth parameterization to formulate the specific strain energy function of the solid under analysis as a combination of linear-based ψ_L and nonlinear-based ψ_{NL} specific strain energy functions, as follows

$$\psi(\mathbf{u}_e) = \left[\psi_{NL}(\gamma_e \mathbf{u}_e) - \psi_L(\gamma_e \mathbf{u}_e) + \psi_L(\mathbf{u}_e)\right] f_k(\overline{\rho}_e), \tag{7}$$

where $\psi(\mathbf{u}_e)$ is the specific strain energy function of element e, which depends on the local displacement vector $\mathbf{u}_e$; $f_k(\overline{\rho}_e)$ is the SIMP (Solid Isotropic Material with Penalization) stiffness interpolation function [50, 51], defined as $f_k(\overline{\rho}_e) = \rho_{min} + (1 - \rho_{min})\overline{\rho}_e^p$, with $p = 3$ in this paper; and γ_e is a smoothed Heaviside approximation function, defined as

$$\gamma_e = \frac{\tanh\left(\beta_\gamma \eta_\gamma\right) + \tanh\left(\beta_\gamma\left(\overline{\rho}_e^p - \eta_\gamma\right)\right)}{\tanh\left(\beta_\gamma \eta_\gamma\right) + \tanh\left(\beta_\gamma\left(1 - \eta_\gamma\right)\right)}. \tag{8}$$

The smoothed Heaviside approximation used in Equation (8), to interpolate the specific strain energy function, is the same employed in Equation (2) to compute the relative densities; different parameters are used, though. In Equation (8), β_γ controls the non-linearity and η_γ the projection level of the smoothed Heaviside approximation. By defining a large positive value for β_γ and a small positive value for η_γ, one can ensure a linear behavior for the low density regions and a nonlinear behavior otherwise, thus alleviating the convergence issues associated with the excessive deformation in the void regions. In this paper, we follow the hints presented by [4], and we set $\beta_\gamma = 500$ and $\eta_\gamma = 0.01$ as fixed parameters during the whole optimization procedure.

3.2. Specific strain energy function

In this subsection, index notation is employed. The following neo-Hookean specific strain energy function, proposed by [52, 53], and employed by [14] in compliance-based topology optimization, is employed in this paper to model the geometric nonlinear behavior of the structure

$$\psi_{NL} = \lambda\left(\frac{J^2 - 1}{4}\right) - \left(\frac{\lambda}{2} + \mu\right)\ln J + \frac{1}{2}\mu\left(C_{kk} - 3\right), \tag{9}$$

where λ and μ are the Lamé constants, J is the determinant of the deformation gradient A_{ij}, and C_{kk} is the trace of the right Cauchy-Green deformation tensor $C_{ij} = A_{ki}A_{kj}$. The right Cauchy-Green deformation tensor is used to compute the Green strain tensor as

$$E_{ij} = \frac{1}{2}\left(C_{ij} - \delta_{ij}\right), \tag{10}$$

where δ_{ij} is the Kronecker delta.

The second Piola–Kirchhoff stress is computed by the derivative of the specific strain energy function, Equation (9), with respect to the Green strain tensor, Equation (10), as follows

$$S_{ij}^{NL} = \frac{\partial \psi_{NL}}{\partial E_{ij}}, \tag{11}$$

and is given by

$$S_{ij}^{NL} = \frac{\lambda}{2}\left(J^2 - 1\right)C_{ij}^{-1} + \mu\left(\delta_{ij} - C_{ij}^{-1}\right), \tag{12}$$

where C_{ij}^{-1} is the ij component of matrix $\mathbf{C}^{-1}$.

For plane stress problems, we have $S_{i3}^{NL} = S_{3j}^{NL} = C_{i3} = C_{3j} = 0$ and $C_{33} \neq 0$. The component C_{33} of the right Cauchy-Green deformation tensor can be obtained by substituting $S_{33}^{NL} = 0$ in Equation (12). After some manipulation, one obtains

$$C_{33} = \frac{\lambda + 2\mu}{\lambda \overline{J}^2 + 2\mu}, \tag{13}$$

where $\overline{J}^2 = C_{11}C_{22} - C_{12}C_{21}$. In order to obtain the analytic expression of the second Piola–Kirchhoff stress for plane stress problems, one can substitute C_{33} in Equation (12), obtaining

$$S_{ij}^{NL} = \frac{\lambda}{2}\left[\frac{\overline{J}^2(\lambda + 2\mu)}{\lambda \overline{J}^2 + 2\mu} - 1\right]C_{ij}^{-1} + \mu\left(\delta_{ij} - C_{ij}^{-1}\right), \tag{14}$$

which holds for $i = 1, 2$ and $j = 1, 2$. The Cauchy stresses are then given by the following expression [9, 54]

$$\hat{\sigma}_{ij}^{NL} = J^{-1} A_{ik} S_{kl}^{NL} A_{jl}. \tag{15}$$

The derivative of the second Piola–Kirchhoff stress, Equation (14), with respect to the Green strain tensor, Equation (10), necessary to solve the resulting system of nonlinear equations with the Newton-Raphson method, can be written as

$$C_{ijkl}^{NL} = \frac{\partial S_{ij}^{NL}}{\partial E_{kl}}, \tag{16}$$

and is given by

$$C^{NL}_{ijkl} = \frac{\lambda}{2}\left\{\frac{4\mu\,\overline{J}^2\,(\lambda+2\mu)}{\left(\lambda\,\overline{J}^2+2\mu\right)^2}C^{-1}_{ij}C^{-1}_{kl} - \left[\frac{\overline{J}^2\,(\lambda+2\mu)}{\lambda\,\overline{J}^2+2\mu} - 1\right]\mathcal{D}_{ijkl}\right\} + \mu\mathcal{D}_{ijkl}, \tag{17}$$

where $\mathcal{D}_{ijkl}$ is given by [9, 54]

$$\mathcal{D}_{ijkl} = -\frac{\partial C^{-1}_{ij}}{\partial E_{kl}} = C^{-1}_{ik}C^{-1}_{jl} + C^{-1}_{il}C^{-1}_{jk}. \tag{18}$$

The specific strain energy function for the linear material model, based on the infinitesimal strain tensor $\boldsymbol{\varepsilon}$, is given by [4]

$$\psi_L = \frac{1}{2}\lambda\varepsilon^2_{kk} + \mu\varepsilon_{ij}\varepsilon_{ij}. \tag{19}$$

Following the same procedure as before, one can compute the first- and second-order derivatives of ψ_L with respect to the infinitesimal strain tensor $\boldsymbol{\varepsilon}$. For plane stress problems, the following expressions are obtained for the Cauchy stress

$$\hat{\sigma}^L_{ij} = \frac{2\mu\lambda}{\lambda+2\mu}\overline{\varepsilon}_{kk}\delta_{ij} + 2\mu\varepsilon_{ij}, \tag{20}$$

where $\overline{\varepsilon}_{kk} = \varepsilon_{11} + \varepsilon_{22}$, and for the material elasticity tensor

$$C^L_{ijkl} = \frac{\partial\hat{\sigma}^L_{ij}}{\partial\varepsilon_{kl}} = \frac{2\mu\lambda}{\lambda+2\mu}\delta_{ij}\delta_{kl} + \mu\left(\delta_{ik}\delta_{jl} + \delta_{il}\delta_{jk}\right). \tag{21}$$

3.3. Positional numerical procedure

In this paper, we employ the finite element method based on nodal positions $\mathbf{Y}$, instead of nodal displacements $\mathbf{U}$, following [55–57], in order to model the equilibrium configuration of the structural system. Nodal positions are related to nodal displacements as $\mathbf{Y} = \mathbf{U} + \mathbf{X}$, where $\mathbf{X}$ is the global vector of initial positions. Considering a static problem subjected to nodal conservative loads, and a total Lagrangian description, the total potential energy of the system can be written as

$$\Pi = \sum_{e=1}^{N_e}\int_{\Omega_e}\psi(\mathbf{u}_e)\;d\Omega_e - \sum_{i=1}^{N_{dof}} f^{ext}_i y_i, \tag{22}$$

where Ω_e is the domain of integration of element e, f^{ext}_i is the external load at the i-th degree of freedom, y_i is the nodal position associated with the i-th degree of freedom, and N_{dof} is the total number of degrees of freedom of the finite element mesh.

The equilibrium configuration is given by stationarity of the total potential energy of the system, as

$$\delta\Pi = \sum_{a=1}^{N_{dof}}\frac{\partial\Pi}{\partial y_a}\delta y_a = 0, \tag{23}$$

such that $\frac{\partial \Pi}{\partial y_a} = 0$, for $a = 1, 2, ..., N_{dof}$. The derivative of the total potential energy, with respect to a nodal position y_a, is written as

$$\frac{\partial \Pi}{\partial y_a} = \sum_{e=1}^{N_e} \int_{\Omega_e} \frac{\partial \psi\left(\mathbf{u}_e\right)}{\partial y_a} \, d\Omega_e - f_a^{ext}, \tag{24}$$

which gives, in vector form, the following equation

$$\mathbf{R}\left(\mathbf{Y}\right) = \mathbf{F}_{int}\left(\mathbf{Y}\right) - \mathbf{F}_{ext}, \tag{25}$$

where $\mathbf{R}\left(\mathbf{Y}\right)$ is the global vector of nodal residual forces, $\mathbf{Y}$ is the global vector of nodal positions, $\mathbf{F}_{int}\left(\mathbf{Y}\right)$ is the global vector of internal forces, and $\mathbf{F}_{ext}$ is the global vector of external forces.

In order to compute the global vector of internal forces, one has to compute the derivative of the specific strain energy function, Equation (7), with respect to a nodal position y_a, as follows

$$\frac{\partial \psi\left(\mathbf{u}_e\right)}{\partial y_a} = \left[\frac{\partial \psi_{NL}\left(\gamma_e \mathbf{u}_e\right)}{\partial y_a} - \frac{\partial \psi_{L}\left(\gamma_e \mathbf{u}_e\right)}{\partial y_a} + \frac{\partial \psi_{L}\left(\mathbf{u}_e\right)}{\partial y_a}\right] f_k\left(\overline{\rho}_e\right). \tag{26}$$

Each term in the square brackets, Equation (26), is computed through a chain rule, by using the first-order derivatives of nonlinear ψ_{NL} and linear ψ_L specific strain energy functions with respect to $\mathbf{E}$ and $\boldsymbol{\varepsilon}$, respectively. These derivatives are given by Equations (14) and (20), respectively. The derivative shown in Equation (26) is then computed as

$$\begin{aligned}\frac{\partial \psi}{\partial y_a} &= \left[\frac{\partial \psi_{NL}\left(\gamma_e\right)}{\partial \mathbf{E}\left(\gamma_e\right)} : \frac{\partial \mathbf{E}\left(\gamma_e\right)}{\partial y_a} - \frac{\partial \psi_{L}\left(\gamma_e\right)}{\partial \boldsymbol{\varepsilon}\left(\gamma_e\right)} : \frac{\partial \boldsymbol{\varepsilon}\left(\gamma_e\right)}{\partial y_a} + \frac{\partial \psi_{L}}{\partial \boldsymbol{\varepsilon}} : \frac{\partial \boldsymbol{\varepsilon}}{\partial y_a}\right] f_k\left(\overline{\rho}_e\right) \\ &= \left[\mathbf{S}^{NL}\left(\gamma_e\right) : \frac{\partial \mathbf{E}\left(\gamma_e\right)}{\partial y_a} - \hat{\boldsymbol{\sigma}}^{L}\left(\gamma_e\right) : \frac{\partial \boldsymbol{\varepsilon}\left(\gamma_e\right)}{\partial y_a} + \hat{\boldsymbol{\sigma}}^{L} : \frac{\partial \boldsymbol{\varepsilon}}{\partial y_a}\right] f_k\left(\overline{\rho}_e\right),\end{aligned} \tag{27}$$

where the dependence on $\mathbf{u}_e$ was omitted for simplicity, and the symbol " : " means double contraction.

The resulting system of nonlinear equations, given by $\mathbf{R}\left(\mathbf{Y}\right) = \mathbf{0}$, is solved with the Newton-Raphson method, requiring computation of the Jacobian matrix of the global residual forces, denoted by $\frac{\partial R(\mathbf{Y})}{\partial \mathbf{Y}}$. In order to compute this matrix, one has to compute the derivative of $\frac{\partial \psi}{\partial y_a}$, Equation (27), necessary in the assembling process of the internal forces, Equation (24), with respect to a nodal position y_b. This derivative is given by

$$\begin{aligned}\frac{\partial^2 \psi}{\partial y_a \partial y_b} = &\left[\frac{\partial \mathbf{E}\left(\gamma_e\right)}{\partial y_a} : \frac{\partial \mathbf{S}^{NL}\left(\gamma_e\right)}{\partial \mathbf{E}\left(\gamma_e\right)} : \frac{\partial \mathbf{E}\left(\gamma_e\right)}{\partial y_b} + \mathbf{S}^{NL}\left(\gamma_e\right) : \frac{\partial^2 \mathbf{E}\left(\gamma_e\right)}{\partial y_a \partial y_b}\right. \\ &\left. - \frac{\partial \boldsymbol{\varepsilon}\left(\gamma_e\right)}{\partial y_a} : \frac{\partial \hat{\boldsymbol{\sigma}}^{L}\left(\gamma_e\right)}{\partial \boldsymbol{\varepsilon}\left(\gamma_e\right)} : \frac{\partial \boldsymbol{\varepsilon}\left(\gamma_e\right)}{\partial y_b} + \frac{\partial \boldsymbol{\varepsilon}}{\partial y_a} : \frac{\partial \hat{\boldsymbol{\sigma}}^{L}}{\partial \boldsymbol{\varepsilon}} : \frac{\partial \boldsymbol{\varepsilon}}{\partial y_b}\right] f_k\left(\overline{\rho}_e\right).\end{aligned} \tag{28}$$

4. Proposed stress interpolation scheme

In finite strain theory, the Cauchy stress tensor is related to the second Piola-Kirchhoff stress tensor through Equation (15). The second Piola-Kirchhoff stress tensor, in turn, is obtained through the derivative of the specific strain energy function with respect to the Green strain tensor, Equation (11). In infinitesimal strain theory, on the other hand, one can directly obtain the Cauchy stress tensor with Equation (20), which is the derivative of the specific strain energy function with respect to the infinitesimal strain tensor.

In this paper, the specific strain energy function, Equation (7), is defined in such way as to alleviate the convergence issues associated with the low density regions under large deformation, by modeling these regions with linear analysis. Since we are using the energy interpolation scheme, it is necessary to employ some additional scheme to interpolate the solid Cauchy stress tensor, to avoid its computation with the nonlinear formulation at regions modeled with the linear formulation. Based on the already employed interpolation function used in the energy interpolation scheme, we propose to compute the Cauchy stress tensor as

$$\hat{\boldsymbol{\sigma}}_{(k)} = \gamma_k \hat{\boldsymbol{\sigma}}^{NL}_{(k)} + (1 - \gamma_k)\, \hat{\boldsymbol{\sigma}}^{L}_{(k)}, \tag{29}$$

where $\hat{\boldsymbol{\sigma}}_{(k)}$ is the solid Cauchy stress tensor at point k, γ_k is the smoothed Heaviside interpolation function defined in Equation (8), $\hat{\boldsymbol{\sigma}}^{NL}_{(k)}$ is the solid Cauchy stress tensor obtained using the finite strain theory, and $\hat{\boldsymbol{\sigma}}^{L}_{(k)}$ is the solid Cauchy stress tensor obtained using the infinitesimal strain theory. The components of the solid Cauchy stress tensor considering the linear analysis, $\hat{\boldsymbol{\sigma}}^{L}_{(k)}$, are obtained with Equation (20), whereas the components of $\hat{\boldsymbol{\sigma}}^{NL}_{(k)}$ are obtained with Equation (15).

By employing the proposed stress interpolation scheme, Equation (29), we have $\hat{\boldsymbol{\sigma}}_{(k)} = \hat{\boldsymbol{\sigma}}^{NL}_{(k)}$ for $\gamma_k = 1$, and $\hat{\boldsymbol{\sigma}}_{(k)} = \hat{\boldsymbol{\sigma}}^{L}_{(k)}$ for $\gamma_k = 0$. That is, the stresses in solid regions are computed with the nonlinear model, whereas the stresses in the void regions are computed with the linear analysis. It is important to mention that the stresses in the void regions are mostly zero, due to the stress constraint relaxation (ε-relaxed approach); thus, in these regions no accurate modeling of stresses is required. Moreover, in the results section, the body-fitted post-processing scheme is performed over the optimized structures considering a full nonlinear modeling, and a good fit is observed between pixel-based and body-fitted stress responses, confirming that the proposed stress interpolation does not deteriorate the stress response of the solid regions.

5. Optimization strategy

In addition to the challenges originated from use of the finite strain theory, the proposed formulation is also subjected to the main challenges arising from the consideration of stress constraints: the singularity phenomenon and the large number of constraints. The singularity phenomenon is handled by use of the ε-relaxed scheme, as presented in subsection 2.1.2. The large number of stress constraints may be handled by use of aggregation techniques [17, 21, 33], active set strategies [15, 20], or some alternative technique, as the augmented Lagrangian method [16, 58]. In this paper, we use the augmented Lagrangian method to solve both the maximum output displacement and the path-generating problems, following [35]. We use the augmented Lagrangian formulation presented in [59].

The augmented Lagrangian method is employed to replace the original constrained optimization problem by a series of bound constrained optimization subproblems. The subproblems associated with the maximum output displacement problem, Equation (1), are given by

$$\begin{array}{lll} \underset{\rho}{\text{Min.}} & L\left(\overline{\boldsymbol{\rho}}^{(e)}, \overline{\boldsymbol{\rho}}^{(i)}, \overline{\boldsymbol{\rho}}^{(d)}, \boldsymbol{\mu}, \mathbf{r}\right) & \\ & \mathbf{R}\left(\mathbf{Y}\left(\overline{\boldsymbol{\rho}}^{(j)}\right)\right) = \mathbf{0} & j \in \{e, i, d\} \\ & 0 \leqslant \rho_e \leqslant 1 & e = 1, 2, ..., N_e \end{array} , \tag{30}$$

where $L\left(\overline{\boldsymbol{\rho}}^{(e)}, \overline{\boldsymbol{\rho}}^{(i)}, \overline{\boldsymbol{\rho}}^{(d)}, \boldsymbol{\mu}, \mathbf{r}\right)$ is the augmented Lagrangian function, given by the objective function of the original problem weighted by both volume and stress constraints, $\boldsymbol{\mu}$ is a vector which contains all Lagrange multipliers of the problem, and $\mathbf{r}$ is a vector which contains all penalization parameters of the problem. The subproblems associated with the path-generating problem, Equation (6), can also be represented by Equation (30), replacing $\overline{\boldsymbol{\rho}}^{(j)}$ with $\overline{\overline{\boldsymbol{\rho}}}^{(j)}$.

Next subsections present the augmented Lagrangian function for the maximum output displacement and the path-generating optimization problems.

5.1. Maximum output displacement formulation

In our implementations, we make use of the Kreisselmeier–Steinhauser (KS) function [60] to replace the maximum operator applied on the output displacements, in order to allow use of a gradient-based algorithm to solve the optimization subproblems. The smoothened approximation for the maximum operator is given by

$$u_{out}^{KS}\left(\overline{\boldsymbol{\rho}}^{(e)}, \overline{\boldsymbol{\rho}}^{(i)}, \overline{\boldsymbol{\rho}}^{(d)}\right) = \frac{1}{P} \ln\left(\sum_{j \in \{e,i,d\}} \exp\left(P\, u_{out}\left(\overline{\boldsymbol{\rho}}^{(j)}\right)\right)\right), \tag{31}$$

with $u_{out}^{KS}\left(\overline{\boldsymbol{\rho}}^{(e)}, \overline{\boldsymbol{\rho}}^{(i)}, \overline{\boldsymbol{\rho}}^{(d)}\right) \to \max\left(u_{out}\left(\overline{\boldsymbol{\rho}}^{(e)}\right), u_{out}\left(\overline{\boldsymbol{\rho}}^{(i)}\right), u_{out}\left(\overline{\boldsymbol{\rho}}^{(d)}\right)\right)$ for $P \to \infty$. In this paper, we use $P = 10$, since this value provides a good compromise between accuracy and smoothness in the numerical examples addressed. One alternative to the KS function is the bound formulation [61], which was developed to alleviate the non-differentiability of min-max problems.

The augmented Lagrangian function is then given by

$$
\begin{aligned}
L\left(\overline{\boldsymbol{\rho}}^{(e)},\overline{\boldsymbol{\rho}}^{(i)},\overline{\boldsymbol{\rho}}^{(d)},\boldsymbol{\mu},\mathbf{r}\right) =& \frac{k_{in}}{f_{in}} u_{out}^{KS}\left(\overline{\boldsymbol{\rho}}^{(e)},\overline{\boldsymbol{\rho}}^{(i)},\overline{\boldsymbol{\rho}}^{(d)}\right) + k_v V_f\left(\overline{\boldsymbol{\rho}}^{(d)}\right) + \frac{r_{up}}{2}\left\langle \frac{\mu_{up}}{r_{up}} + \frac{V_f\left(\overline{\boldsymbol{\rho}}^{(d)}\right)}{V_{up}^{(d)}} - 1 \right\rangle^2 \\
&+ \frac{r_{low}}{2}\left\langle \frac{\mu_{low}}{r_{low}} - \frac{V_f\left(\overline{\boldsymbol{\rho}}^{(d)}\right)}{V_{low}^{(d)}} + 1 \right\rangle^2 + \frac{r}{2}\sum_{k=1}^{N_k}\left(\left\langle \frac{\mu_k^{(d)}}{r} + \frac{\sigma_{eq}^{(k)}\left(\overline{\boldsymbol{\rho}}^{(d)}\right)}{\sigma_y} - 1 \right\rangle^2\right. \\
&\left.+\left\langle \frac{\mu_k^{(i)}}{r} + \frac{\sigma_{eq}^{(k)}\left(\overline{\boldsymbol{\rho}}^{(i)}\right)}{\sigma_y} - 1 \right\rangle^2 + \left\langle \frac{\mu_k^{(e)}}{r} + \frac{\sigma_{eq}^{(k)}\left(\overline{\boldsymbol{\rho}}^{(e)}\right)}{\sigma_y} - 1 \right\rangle^2\right),
\end{aligned}
\tag{32}
$$

where $\langle\cdot\rangle = \max(0,\cdot)$, $\boldsymbol{\mu}$ contains the Lagrange multipliers: μ_{up}, associated with the upper volume constraint; μ_{low}, associated with the lower volume constraint; $\mu_k^{(j)}$, for $j \in \{e,i,d\}$ and $k = 1,2,...,N_k$, associated with the stress constraints; and $\mathbf{r}$ contains the penalization parameters: r_{up}, associated with the upper volume constraint; r_{low}, associated with the lower volume constraint; r, associated with all stress constraints.

In this paper, we follow the strategy presented in [35] in order to update the Lagrange multipliers $\boldsymbol{\mu}$, penalization parameters $\mathbf{r}$, upper volume fraction $V_{up}^{(d)}$, and parameter β associated with the threshold projection, with the exact same numerical parameters. In order to solve the optimization subproblems, the steepest descent method with move limits is employed [62], with same parameters as described in [35]. Sensitivity analysis is shown in the appendix.

5.2. Path-generating formulation

The augmented Lagrangian function associated with the path-generating design problem, Equation (6), is given by

$$
\begin{aligned}
L\left(\overline{\overline{\boldsymbol{\rho}}}^{(e)},\overline{\overline{\boldsymbol{\rho}}}^{(i)},\overline{\overline{\boldsymbol{\rho}}}^{(d)},\boldsymbol{\mu},\mathbf{r}\right) =& \left(\frac{k_{in}}{f_{in,M}}\right)^2 \sum_{j\in\{e,i,d\}}\sum_{m=1}^{M}\left(u_{out,m}\left(\overline{\overline{\boldsymbol{\rho}}}^{(j)}\right) - u_{out,m}^{*}\right)^2 + \frac{r_{up}}{2}\left\langle \frac{\mu_{up}}{r_{up}} + \frac{V_f\left(\overline{\overline{\boldsymbol{\rho}}}^{(d)}\right)}{V_{up}^{(d)}} - 1 \right\rangle^2 \\
&+ \frac{r}{2}\sum_{k=1}^{N_k}\left(\left\langle \frac{\mu_k^{(d)}}{r} + \frac{\sigma_{eq}^{(k)}\left(\overline{\overline{\boldsymbol{\rho}}}^{(d)}\right)}{\sigma_y} - 1 \right\rangle^2 + \left\langle \frac{\mu_k^{(i)}}{r} + \frac{\sigma_{eq}^{(k)}\left(\overline{\overline{\boldsymbol{\rho}}}^{(i)}\right)}{\sigma_y} - 1 \right\rangle^2 + \left\langle \frac{\mu_k^{(e)}}{r} + \frac{\sigma_{eq}^{(k)}\left(\overline{\overline{\boldsymbol{\rho}}}^{(e)}\right)}{\sigma_y} - 1 \right\rangle^2\right).
\end{aligned}
\tag{33}
$$

In order to solve the subproblems resulting from the path-generating problem, we use the same updating strategy, with same numerical parameters, and the same algorithm employed in the maximum output displacement design problem. Sensitivity analysis is shown in the appendix.

6. Numerical results and discussion

This section presents some numerical investigations performed over two test problems [3]: (a) the inverter problem; and (b) the gripper problem; see Figure 1. Subsection 2.1 presents results obtained with the maximum output displacement formulation, Equation (1). Section 2.2 presents results obtained with the path-generating formulation, Equation (6).

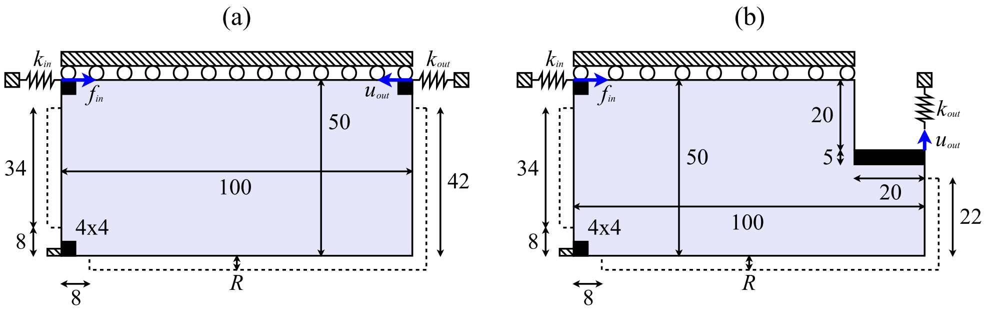

Figure 1: Inverter (a) and Gripper (b) design problems. Support regions on the bottom left of both design domains have size equal to 1. Square-shaped fixed solid regions have size equal to 4×4.

Input data are taken from [35] with minor modifications. Mechanic and geometric properties: Young's Modulus of 1, Poisson's ratio of 0.3, thickness of 1, applied load $f_{in} = 5$, and input stiffness $k_{in} = 1$. The output stiffness is considered as: a) $k_{out} = 0.001$, for the inverter problem; and b) $k_{out} = 0.005$, for the gripper problem.

Input data associated with filter, projection levels and design constraints are presented in each subsection. Input data associated with the optimization algorithm, as penalization parameters and Lagrange multipliers updating scheme, are taken from [35] without modifications, and are not repeated herein. The reader is thus invited to check [35] for additional information.

Additional relevant data: four-node bi-linear square elements are employed to discretize the design domains. The von Mises equivalent stresses are evaluated at the centroid of each finite element. The filter boundary padding [63] is employed to alleviate boundary effects that may occur due to filtering, by extending the design domain with void elements (dashed regions in Figure 1), which are not considered in the analyses, only during filter application.

Both design domains are filled with fixed solid areas in load and support regions, as indicated in Figure 1. The stresses at these regions are set to zero, and thus not taken into account by the algorithm during the optimization procedure.

Both the pixel-based and body-fitted post-processing schemes are employed to verify the accuracy of von Mises stresses and output displacements of the optimized designs [34, 35]. The pixel-based post-processing scheme is performed with the same mesh and same stress interpolation functions used in the optimization procedure; whereas the body-fitted scheme is performed considering a full nonlinear model, Equation (9), over finite element models with smooth boundaries. These are obtained with software Gmsh [64], and are comprised of six-node triangle elements. In the body-fitted cases, the smooth contour plots are directly extracted from the optimized filtered fields. In both cases, the von Mises equivalent stresses are computed at the centroid of each element.

6.1. Maximum output displacement design problem

Input data employed in the min-max optimization procedure: $V_{up} = 0.3$ and $V_{low} = 0.2$ as upper and lower volume fractions, respectively; initial value of design variables of $\rho_e^{(1)} = 0.3$, for $e = 1, 2, ..., N_e$; filter's radius of $R = 2.8$; finite element meshes with $N_e = 80,000$ (inverter) and $N_e = 73,600$ (gripper) elements (i.e., 400×200 elements). Parameter $\beta^{(1)} = 1$ is updated up to a maximum value $\beta_{max} = 11.2$, which corresponds to $\beta_{max} = \beta_{lim}/2$ [35]. Parameters η_d, η_i and η_e are chosen as: 0.25, 0.5 and 0.75 (inverter); and 0.4, 0.5 and 0.6 (gripper).

The Newton-Raphson method is employed, with 3 load increments, in order to find the equilibrium configuration of the structure at each step of the optimization procedure. Convergence is reached when the ratio between the Euclidean norm of vectors of incremental and initial positions is smaller than 1×10^{-6}.

The inverter problem is solved for three situations regarding the stress constraints: no stress constraint; $\sigma_y = 0.05$; and $\sigma_y = 0.03$. Figures 2, 3 and 4 show the optimized topologies (eroded, intermediate and dilated), pixel-based von Mises stresses and body-fitted von Mises stresses, respectively, for the maximum output displacement inverter problem. Topologies and stresses are shown in deformed configuration. A gray rectangle is included below each figure to serve as reference to the undeformed design domain. Convergence histories are shown in Figure 5.

Figures 6 and 7 show the post-processing graphs for maximum von Mises stresses and output displacements, respectively. Both graphs are plotted for η from $\eta_d = 0.25$ to $\eta_e = 0.75$. The pixel-based graphs (solid lines) are obtained for incremental steps of 0.01, and the body-fitted graphs (points) are obtained for incremental steps of 0.05.

Analyzing stress and displacement post-processing graphs, Figures 6 and 7, respectively, one can verify a good fit between pixel-based and body-fitted responses. One can clearly verify that the compromise relation between maximum von Mises stresses and output displacements, observed in [35] for the linear case, is also observed herein: the smaller the value of σ_y, the smaller the output displacement of the resulting mechanism, in absolute value. It is also interesting to note that, whereas rapidly varying stress behavior is obtained for the case with no stress constraint, smooth stress behavior after uniform boundary variation is obtained for both cases in which a stress constraint is applied. Maximum stress constraint violations, $\frac{\sigma_{max}}{\sigma_y} - 1$, are given by: 1.20% (pixel) and 6.65% (fitted), for $\sigma_y = 0.05$; and 2.20% (pixel) and 10.89% (fitted), for $\sigma_y = 0.03$.

Analyzing Figures 3 and 4, one can observe a good agreement between the overall quality of pixel-based and body-fitted von Mises stress fields. It is observed that the smaller the value of σ_y, the more distributed the von Mises

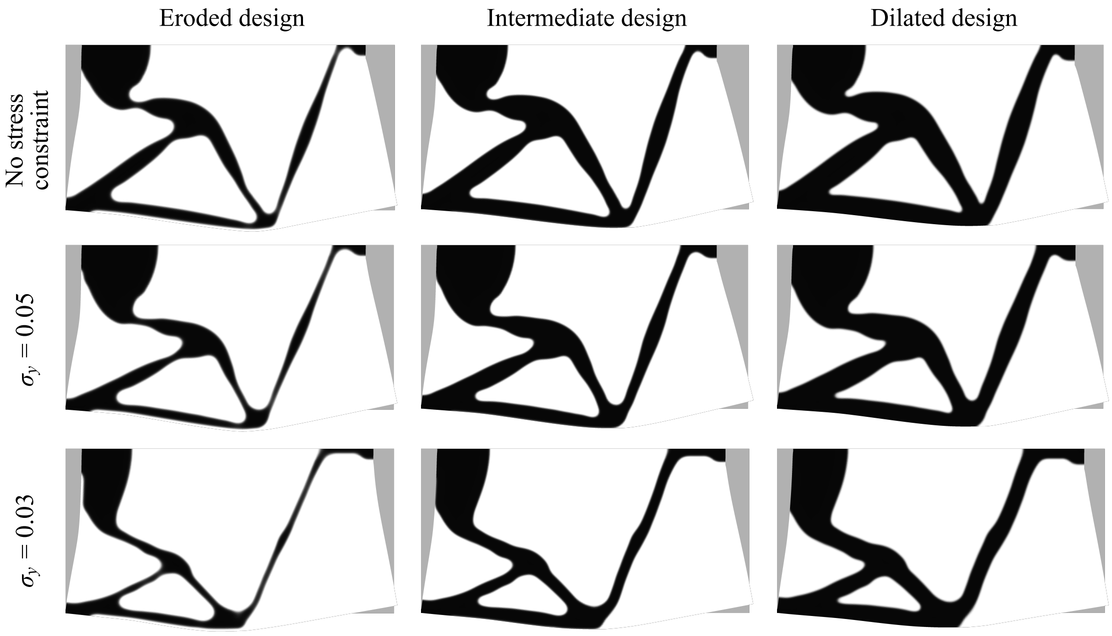

Figure 2: Maximum output displacement inverter problem. Optimized topologies for three levels of stress constraints: no stress constraint; $\sigma_y = 0.05$; and $\sigma_y = 0.03$.

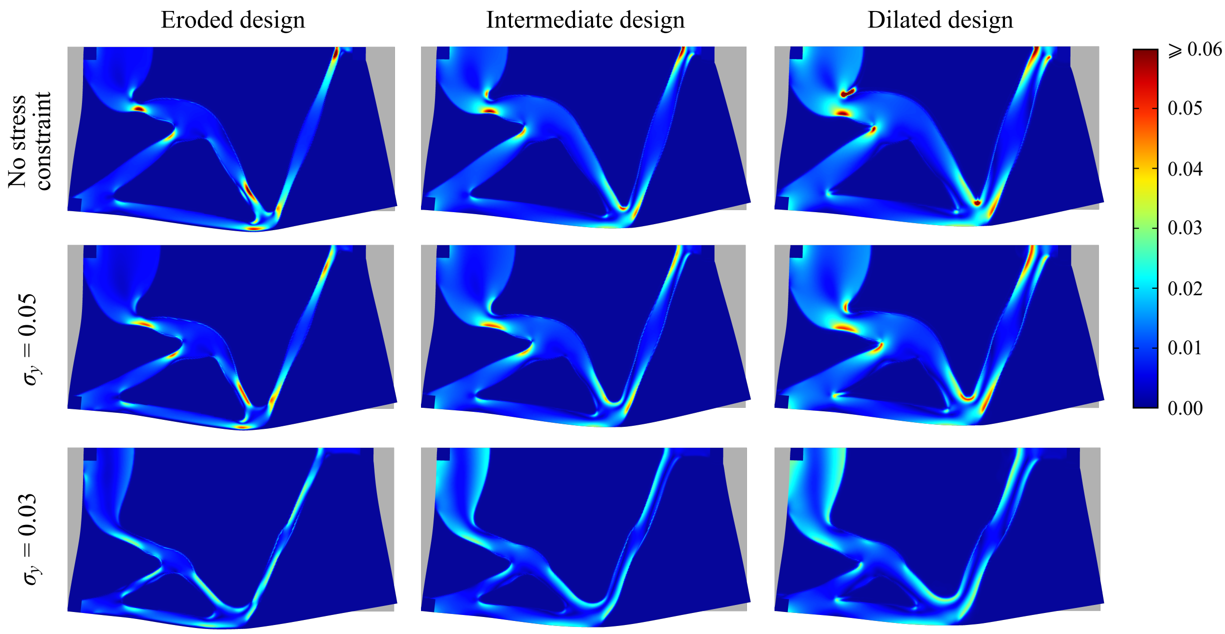

Figure 3: Maximum output displacement inverter problem. Pixel-based von Mises stresses for the structures from Figure 2.

stresses are. Figure 2 shows the optimized topologies in deformed configuration. All structures have the same topology; however, differences in shape are observed. These differences are necessary to alleviate the von Mises stresses at some highly stressed regions, as clearly observed for the dilated topology, where the link between the structural member that

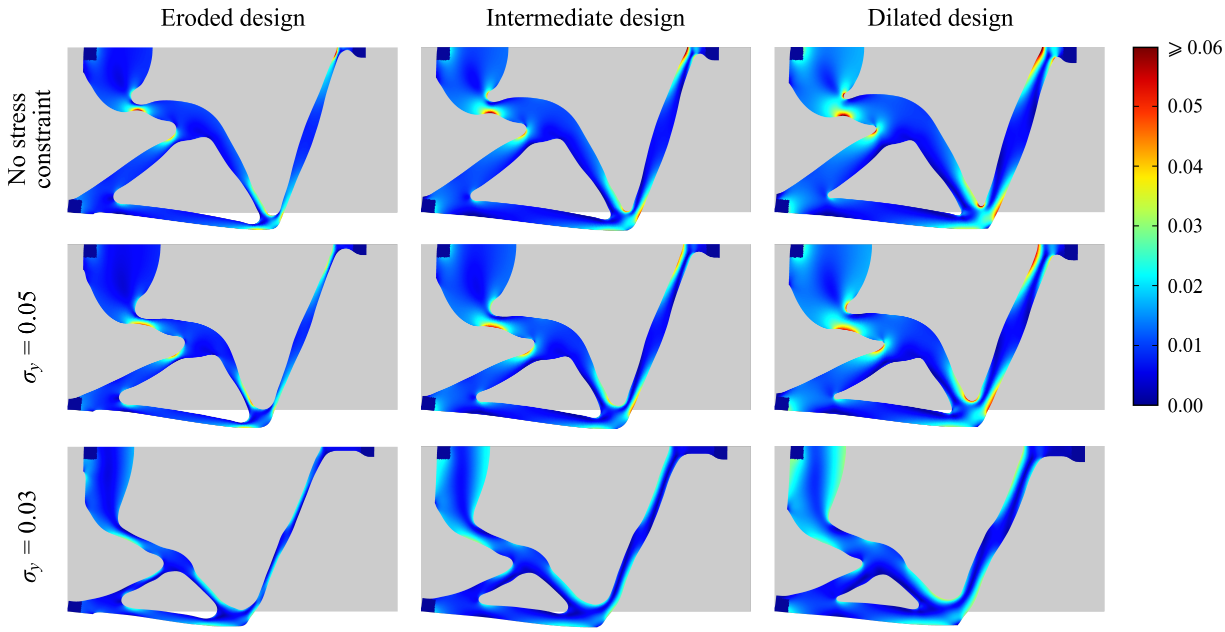

Figure 4: Maximum output displacement inverter problem. Body-fitted von Mises stresses for the structures from Figure 2.

connects the output and the body of the inverter becomes more rounded as the value of σ_y decreases, confirming the results by [35] obtained for the linear cases.

Analyzing Figure 2, one can observe that the optimized topology becomes thinner and thinner, as the value of σ_y is decreased, also confirming the results in [35]. The volume fractions of the resulting intermediate topologies are: $V_f = 0.2861$, for the unconstrained stress case; $V_f = 0.2769$, for $\sigma_y = 0.05$; and $V_f = 0.2163$, for $\sigma_y = 0.03$; satisfying both upper and lower volume fractions, $V_{up} = 0.3$ and $V_{low} = 0.2$.

Analyzing Figure 5, one can observe that the stress-constrained problems need more iterations to satisfy convergence criteria (580 iterations, for $\sigma_y = 0.03$; and 585 iterations, for $\sigma_y = 0.05$), when compared to the problem with no stress constraint (421 iterations). This is justified, since stress constraints introduce additional nonlinearity that should be handled by the optimizer. It is also interesting to note the behavior of the maximum stresses over the iterations: while the stresses of eroded, intermediate and dilated mechanisms are unpredictable and different from each other in the case with no stress constraints, they become uniform and equal to the yield stress in the constrained cases. In the convergence of the output displacements, there is a tendency of rapidly increasing during the first iterations, and then the output displacement of the intermediate topology starts to slightly overcome the outputs from eroded and dilated topologies, as the value of β is updated. This behavior is in agreement with the standard three-field robust approach [37]. In the stress-constrained case for $\sigma_y = 0.03$, one can observe the displacements deteriorate in absolute value after 200 iterations, approximately. This is justified, since very strong stress requirements are imposed; the algorithm

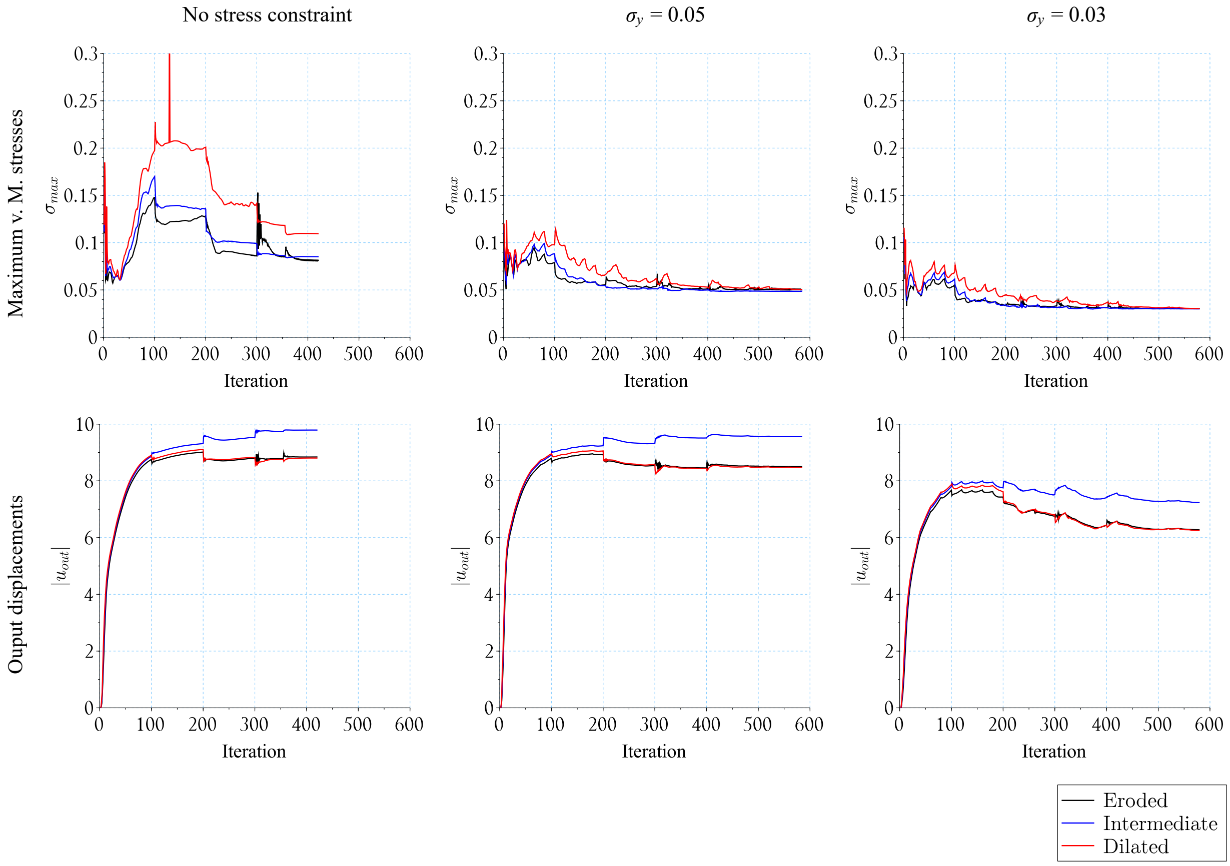

Figure 5: Maximum output displacement inverter problem. Convergence of maximum von Mises stresses (first row) and output displacements (second row), for eroded, intermediate and dilated topologies.

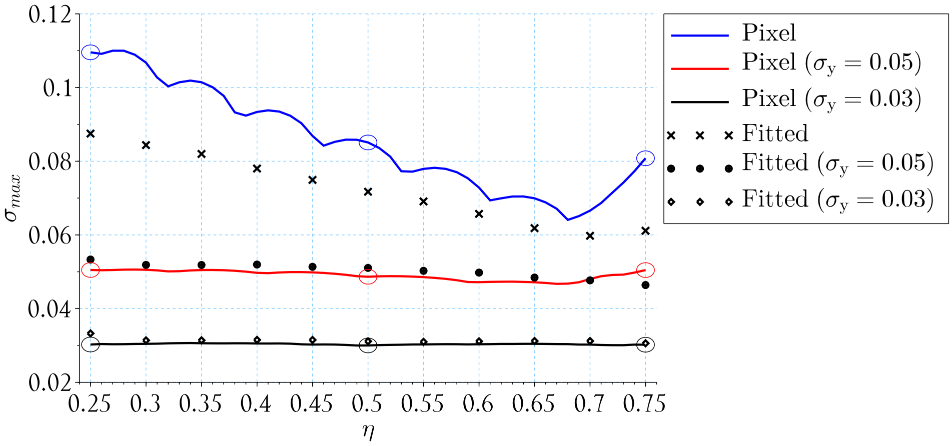

Figure 6: Maximum output displacement inverter problem. Maximum von Mises equivalent stresses for $\eta \in [0.25, 0.75]$ considering both pixel-based and body-fitted nonlinear models.

prioritizes the stress feasibility instead of displacement minimization in this case in order to achieve a feasible solution. It should be noted that the number of iterations is different from the number of objective function evaluations, since we

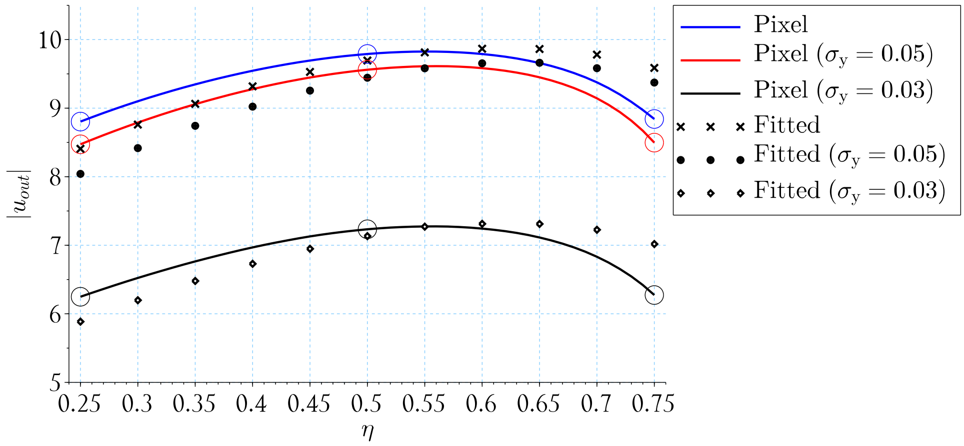

Figure 7: Maximum output displacement inverter problem. Output displacements for $\eta \in [0.25, 0.75]$ considering both pixel-based and body-fitted nonlinear models.

employ the modified steepest descent method with a simple backtracking line search to ensure minimization of the augmented Lagrangian function within a given subproblem. The number of objective function evaluations is: 633, for $\sigma_y = 0.03$; 667, for $\sigma_y = 0.05$; and 500, for the case with no stress constraint.

In order to highlight the importance of the proposed approach, the same inverter problems are solved by employing the standard linear analysis instead, in order to find the equilibrium configuration of the structures at each step of the optimization procedure. Then, the optimized results are post-processed with both pixel-based and body-fitted schemes, considering the same nonlinear material model employed in the nonlinear cases, Equation (9).

Figure 8 shows the optimized intermediate topologies in undeformed configuration for the three stress levels obtained with both nonlinear and linear analyses, and Figure 9 shows the respective von Mises stress and output displacement post-processing graphs. Since a very rapidly varying stress behavior is obtained at the post-processing step of the linear cases, the stress graphs are adjusted with different vertical scales, so the reader can clearly identify the differences between nonlinear and linear responses by analyzing the graphs one by one.

Analyzing Figure 8, one can verify that the same topologies are obtained for nonlinear and linear cases. However, all topologies have different shapes. The effect of these differences can be observed in the post-processing graphs, Figure 9. Contrary to what happens when the nonlinear analysis is employed in the formulation, the optimized designs for the linear analysis are not robust with respect to uniform boundary variations regarding the maximum von Mises stress. Quite the opposite: the stresses have rapidly varying behavior when uniform boundary variation is investigated. Moreover, the results obtained with the nonlinear analysis outperform the results obtained with the linear analysis in all the investigated cases, in both output displacements and maximum von Mises stresses. Maximum stress constraint violations for the linear case, post-processed with the nonlinear analysis: 327.10% (pixel) and 206.27% (fitted), for

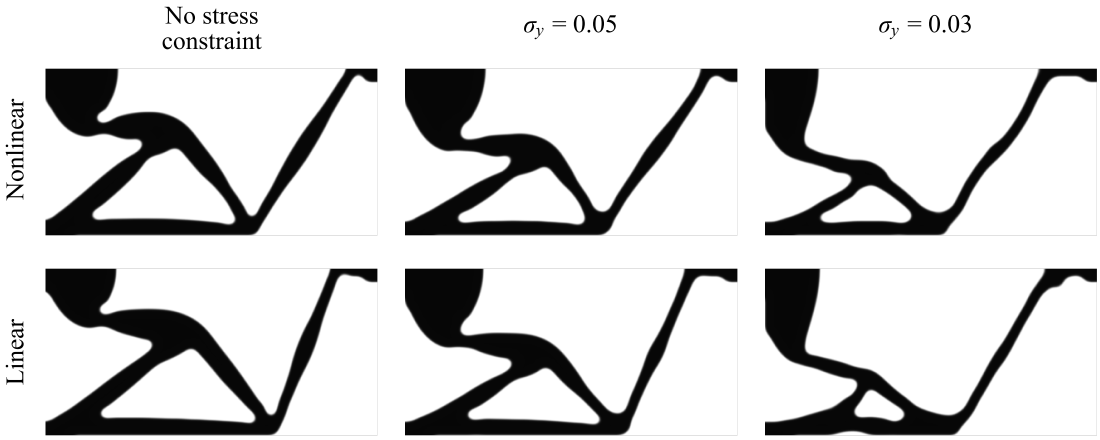

Figure 8: Maximum output displacement inverter problem. Optimized intermediate topologies obtained with the proposed formulation considering nonlinear analysis (first row), and with the formulation considering linear analysis (second row).

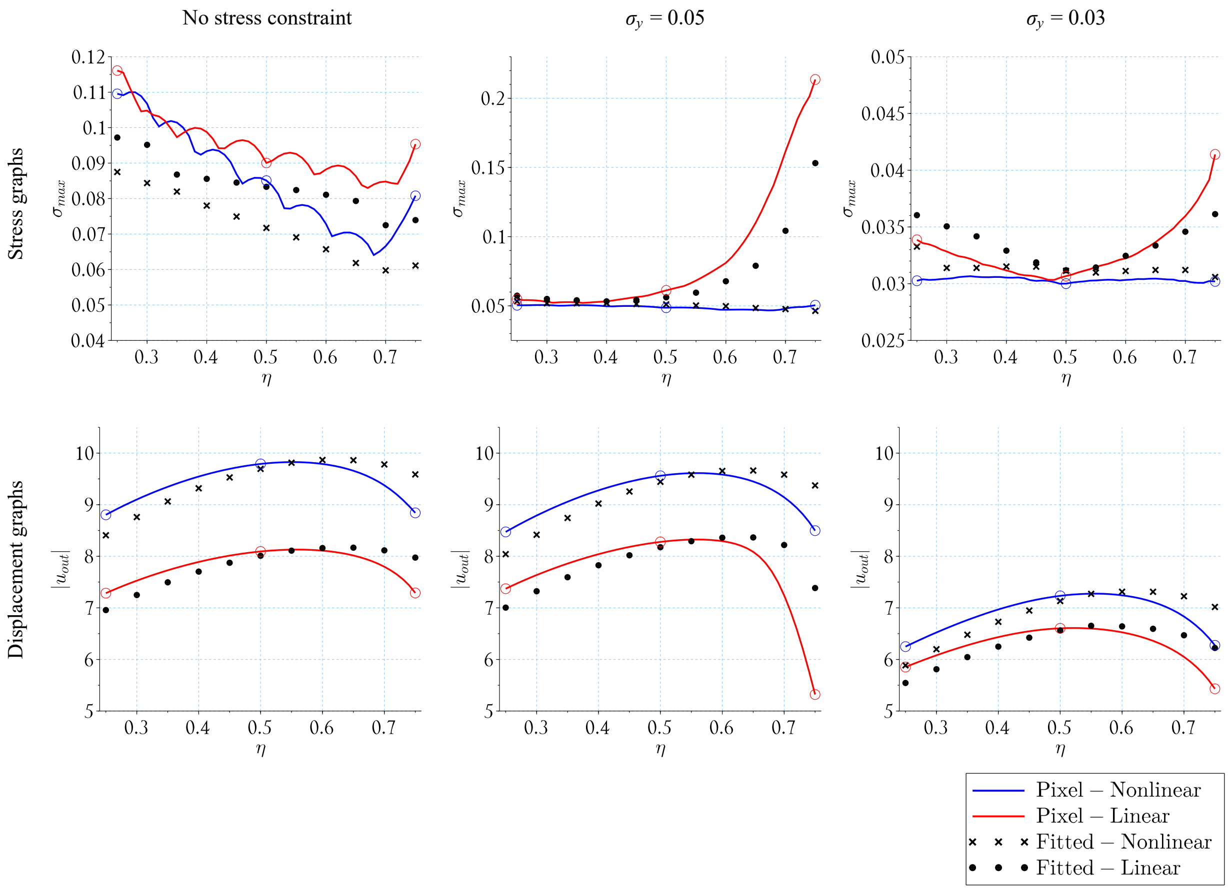

Figure 9: Maximum output displacement inverter problem. Maximum von Mises stress (first row) and output displacement (second row) post-processing graphs. Nonlinear refers to the nonlinear results post-processed with nonlinear analysis, and linear refers to the linear results post-processed with nonlinear analysis.

σ_y = 0.05; and 37.98% (pixel) and 20.44% (fitted), for σ_y = 0.03. Note that these large stress constraint violations are due to use of the nonlinear analysis in the post-processing step; it should be clear that when the post-processing of the linear case is performed with linear analysis, good fits are observed, as shown in [35]. However, it is acknowledged, in the literature, that the linear analysis is not accurate to model structures under large displacements; thus, in such cases, use of the proposed formulation is necessary.

Figure 10 shows the most critical linear case, which presented the largest stress constraint violation (eroded design, for σ_y = 0.05), in deformed configuration. The body-fitted von Mises stresses are shown, and it is observed that although the topologies are the same, a very distinct stress behavior is obtained. There are slight differences in the shape of the mechanism that promote large nonlinear deformations in the linear result, leading mostly to the deterioration of stress performance. This same effect is not observed in the design obtained with nonlinear analysis, since its effect is considered during the whole optimization procedure.

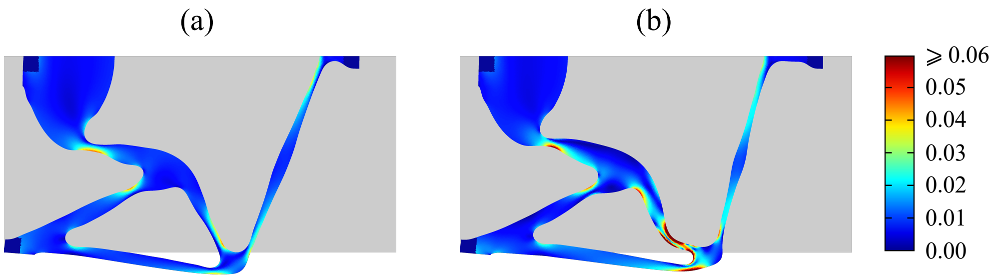

Figure 10: Body-fitted eroded designs, inverter problem, for σ_y = 0.05: (a) solution obtained with the proposed nonlinear approach; (b) solution obtained with the linear approach. Post-processed deformed configuration is obtained with full nonlinear analysis in both cases.

For the sake of completeness, the gripper design problem is solved, Figure 1 (b). A yield stress value of σ_y = 0.04 is considered in this case. The optimized solution is obtained within 540 iterations, and 604 objective function evaluations. Figure 11 shows eroded, intermediate and dilated topologies in deformed configuration. Analyzing the figure, one can observe good agreement between pixel-based and body-fitted von Mises stress fields.

In order to verify the importance of using nonlinear analysis in this case, we also solve the problem considering linear analysis during the optimization procedure. Optimized intermediate topologies, for both nonlinear and linear cases, are shown in Figure 12, in undeformed configuration. Although the same topology is obtained, slight differences in shape can be observed.

Both the nonlinear and linear results are post-processed with use of the body-fitted and pixel-based post-processing schemes. The resulting graphs are shown in Figure 13. The same behavior observed earlier for the inverter case is confirmed in the gripper case: the nonlinear result outperforms the linear result in both stress feasibility and output performance. Moreover, one can verify a very smooth stress behavior after uniform boundary variation in the nonlinear

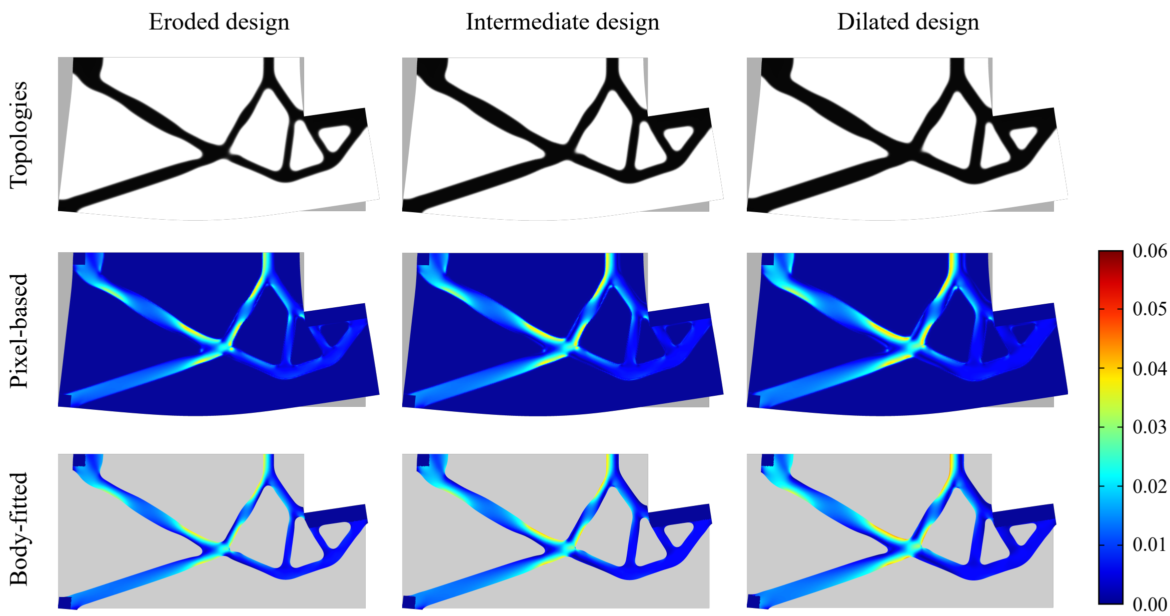

Figure 11: Maximum output displacement gripper problem. Topologies (first row), pixel-based von Mises stresses (second row) and body-fitted von Mises stresses (third row) in deformed configuration, for $\sigma_y = 0.04$.

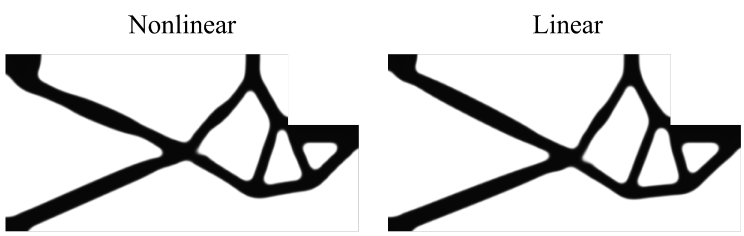

Figure 12: Maximum output displacement gripper problem. Intermediate topologies obtained with the nonlinear (left) and linear (right) analyses.

case. This same behavior is not observed in the linear case, rather the contrary: a very rapidly varying stress behavior is observed, with large stress constraint violation considering the stress limit of $\sigma_y = 0.04$. Maximum stress constraint violations are given by: 0.60% (pixel) and 10.62% (fitted), for the nonlinear case; and 80.86% (pixel) and 55.99% (fitted), for the linear case.

6.2. *Path-generating design problem*

In this subsection, the path-generating problem is investigated. Only the inverter problem is addressed. Input data: upper volume fraction of $V_{up} = 0.25$; initial value of design variables of $\rho_e^{(1)} = 0.3$, for $e = 1, 2, ..., N_e$; filter's radius of $R_2 = 2.8$; finite element mesh with $N_e = 20,000$ (i.e., 200×100 elements). Parameter $\beta_2^{(1)} = 1$ is updated up to a maximum value $\beta_{max} = 11.2$, which corresponds to $\beta_{max} = \beta_{lim}$ [35]. Parameters η_d, η_i and η_e are chosen as: 0.45, 0.5 and 0.55. Parameters R_1, β_1 and η_1, related to the double filter approach, are chosen as: $2R_2$, $2\beta_2$ and η_d; as described

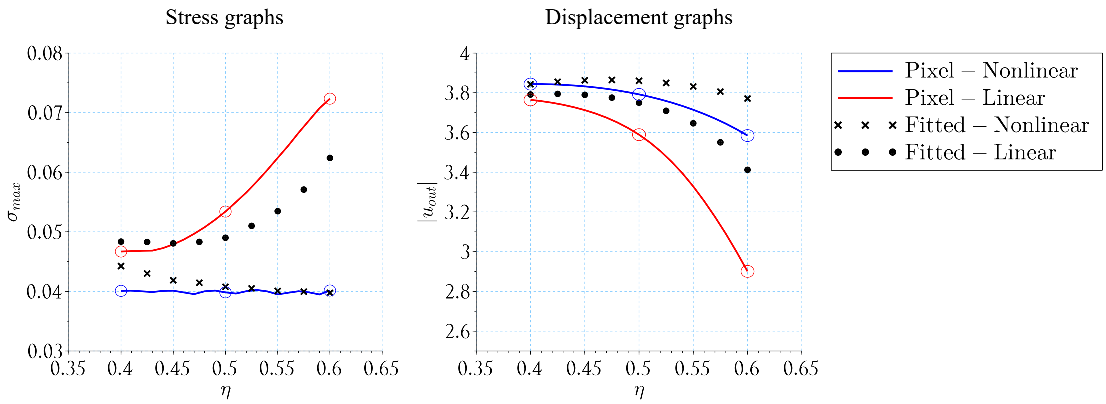

Figure 13: Maximum output displacement gripper problem. Post-processing graphs of maximum von Mises stresses (left) and output displacements (right). Nonlinear refers to the nonlinear results post-processed with nonlinear analysis, and linear refers to the linear results post-processed with nonlinear analysis.

in subsection 2.2.1. The problem is solved for three situations regarding the stress constraints: $\sigma_y = 0.1$; $\sigma_y = 0.05$; and $\sigma_y = 0.03$.

We solve the inverter problem for two sets of control points, proportional (set 1) and non-proportional (set 2), with two control points per set:

1. Output displacements: $u^*_{out,1} = -2.5$ and $u^*_{out,2} = -5.0$; input loads: $f_{in,1} = 2.5$ and $f_{in,2} = 5.0$;
2. Output displacements: $u^*_{out,1} = -3.5$ and $u^*_{out,2} = -5.0$; input loads: $f_{in,1} = 2.5$ and $f_{in,2} = 5.0$.

The difference between both sets is in the first control point. The proportional set requires that the mechanism reaches an output displacement of $u^*_{out,1} = -2.5$ for an input load of $f_{in,1} = 2.5$, whereas the non-proportional set requires an output displacement of $u^*_{out,1} = -3.5$ for the same load magnitude. The output displacement for the final load level, $f_{in,2} = 5.0$, is the same, $u^*_{out,2} = -5.0$. The main goal of the problem is the design of a compliant mechanism that passes through the prescribed control points, while still satisfying the stress requirements, and with minimum error regarding uniform boundary variations. The stress constraints are applied for the second load level only.

In this problem, the Newton-Raphson method is employed with 4 load steps: 2 load steps are first employed to find the equilibrium configuration due to the first load level $f_{in,1} = 2.5$, and the other 2 load steps are due to the second load level $f_{in,2} = 5.0$. The same convergence criterion employed in the maximum output displacement problem is used herein.

The first results presented in this subsection demonstrates the importance of using the double filter procedure to address the proposed path-generating design problem. Figure 14 shows the optimized intermediate topologies and respective computed displacement paths for eroded, intermediate and dilated designs. These results were obtained for the case with stress requirement of $\sigma_y = 0.1$ and the proportional set of control points. The post-processed displacement paths are obtained with the pixel-based meshes and 10 load steps. Both the standard robust procedure, with physical densities represented by $\overline{\rho}$, and the robust procedure with the double filter approach, with physical densities represented by $\overline{\overline{\rho}}$, are employed in this case. The single filter procedure is employed with same filter's radius and same η and β parameters used in the second filter step of the double filter approach.

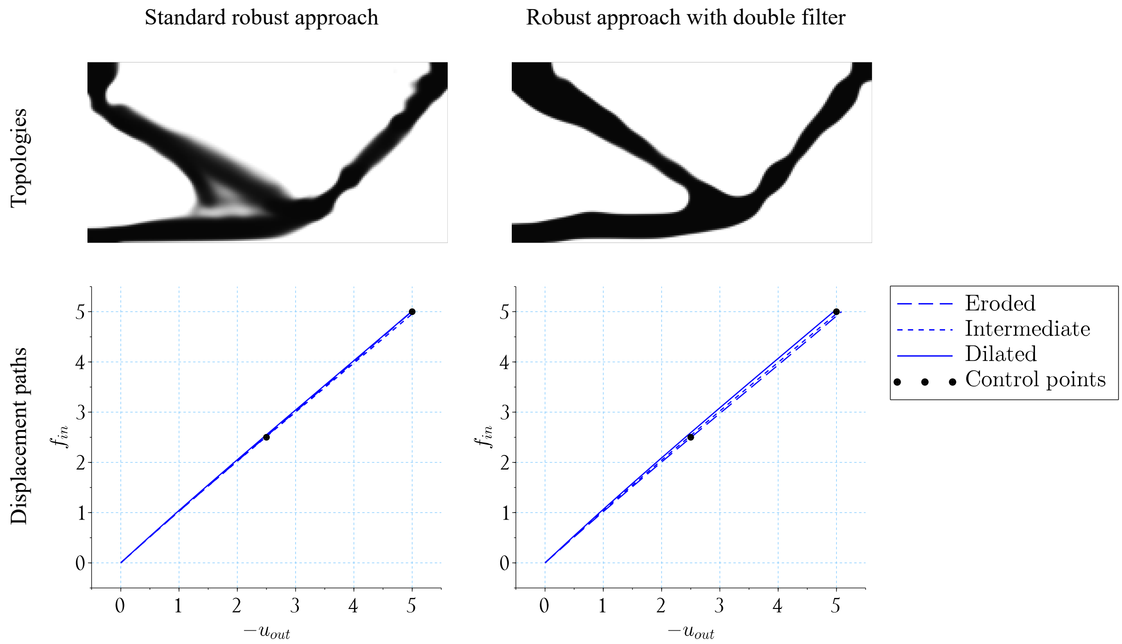

Figure 14: Path-generating inverter problem. Intermediate topologies (first row) and output displacement paths (second row), for the proportional set of control points and $\sigma_y = 0.1$. Standard single filter robust approach (left), and double filter robust approach (right).

Analyzing Figure 14, one can observe that both results have an almost perfect fit between computed displacement paths and prescribed control points; however, the optimized topology obtained with the standard robust procedure (single filter approach) presents large regions of intermediate material, whereas the topology obtained with the robust procedure with double filter approach does not. Intermediate material, in the latter case, is only observed at the transition boundaries between solid and void phases, as expected. From now on, all presented results were obtained with use of the double filter approach.

Figures 15 and 16 show the optimized intermediate topologies in undeformed configuration and the post-processed displacement paths for eroded, intermediate and dilated designs, for both the proportional and non-proportional sets of prescribed control points, respectively. All the post-processed displacement paths are obtained with pixel-based meshes and 10 load steps. Table 1 shows the number of iterations until convergence and the number of objective function evaluations for each problem.

This investigation demonstrates how the optimized paths behave for different stress requirements. We can observe

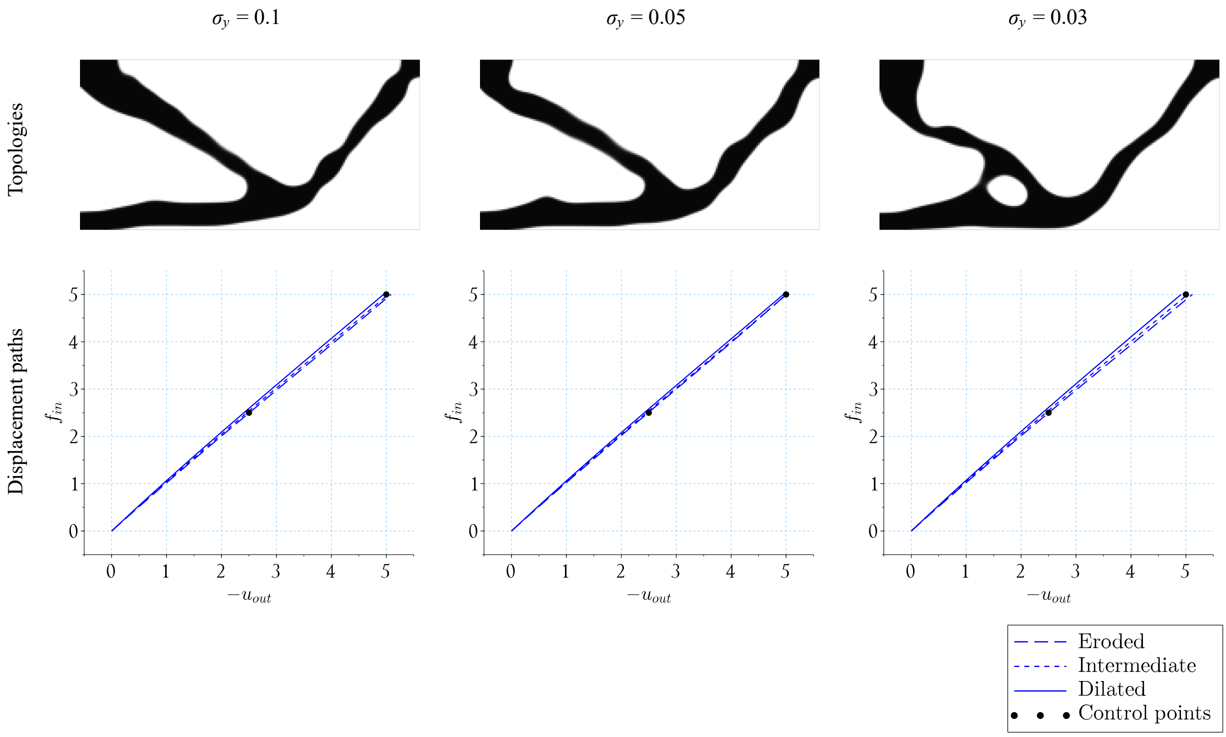

Figure 15: Path-generating inverter problem, proportional set of control points. Intermediate topologies in undeformed configuration (first row), and displacement paths for eroded, intermediate and dilated designs (second row).

Table 1: Path-generating inverter problem. Number of iterations and objective function evaluations to reach convergence criteria, for both proportional and non-proportional set of control points.

	Proportional set		Non-proportional set	
Stress constraint	Iterations	Obj. eval.	Iterations	Obj. eval.
$\sigma_y = 0.1$	151	311	282	400
$\sigma_y = 0.05$	179	397	349	513
$\sigma_y = 0.03$	246	397	393	544

good fit between prescribed and computed paths for both sets of control points, especially for the cases where $\sigma_y = 0.1$ and $\sigma_y = 0.05$ are used. For the cases obtained with $\sigma_y = 0.03$, one can observe a particularly interesting behavior. Whereas for the non-proportional set of points the computed displacement paths start deviating slightly from the prescribed control points, one can verify an almost perfect agreement for the proportional set of points. This behavior is not surprising, since different paths may require different levels of deformation to be achieved. In this case, we observed that the non-proportional set requires more deformation to be achieved, since it corresponds to a nonlinear path with same final displacements as the almost linear path obtained with the proportional set of points.

Analyzing Table 1, two behaviors are observed: (1) the smaller the value of the yield stress, the larger the number of iterations; and (2) the number of iterations related to the proportional set of control points is smaller than its non-proportional counterpart, when the same yield stress is considered. This behavior, however, although intuitive

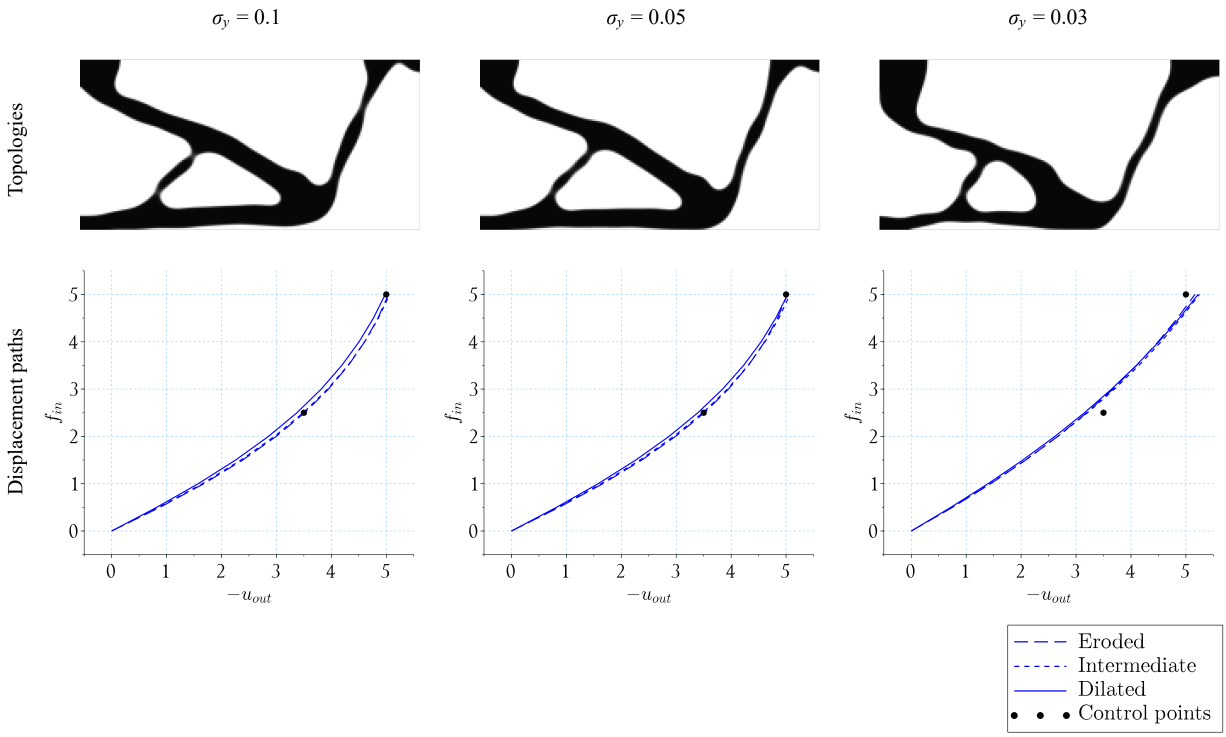

Figure 16: Path-generating inverter problem, non-proportional set of control points. Intermediate topologies in undeformed configuration (first row), and displacement paths for eroded, intermediate and dilated designs (second row).

from a physical point of view, cannot be adopted as a general rule, as demonstrated in subsection 6.1 when solving the maximum output displacement inverter problem for different stress levels.

In order to check for accuracy of displacement paths and for the overall quality of the von Mises stress fields, we employed a body-fitted post processing scheme over eroded, intermediate and dilated optimized topologies. This study is performed over the results obtained for $\sigma_y = 0.05$, for both sets of control points. Figures 17 and 19 show the optimized topologies with respective von Mises stresses, for the proportional and non-proportional sets of control points, respectively. Figures 18 and 20 show the respective output displacement paths.

Analyzing Figures 17 and 19, one can verify good agreement between pixel-based and body-fitted von Misess stresses. Figures 18 and 20 show the output displacement paths for both pixel-based and body-fitted cases, and good agreement is verified as well. A slight deviation between computed and prescribed control points is observed for the non-proportional set of points, in the body-fitted results. However, this slight deviation does not affect the applicability of the approach. Note that, although not performed in this paper, use of finer meshes can help to alleviate the differences between pixel-based and body-fitted results, as demonstrated in [34, 35].

In order to check for stress robustness with respect to uniform boundary variation, the same results for $\sigma_y = 0.05$ are also investigated with the post-processing scheme considering the final applied load of $f_{in,2} = 5.0$, associated with

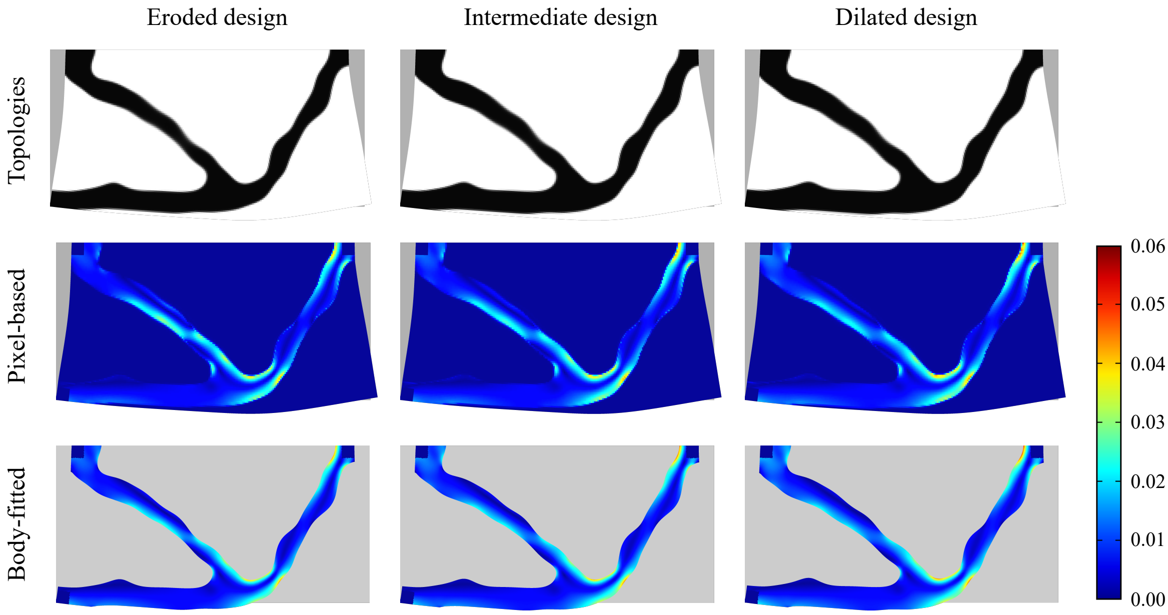

Figure 17: Path-generating inverter problem. Topologies, pixel-based and body-fitted von Mises stresses in deformed configuration, for the proportional set of control points and $\sigma_y = 0.05$.

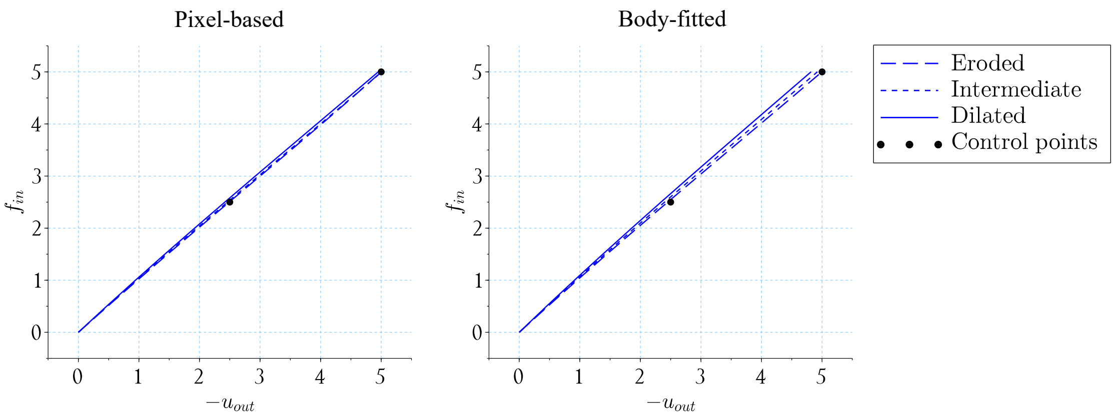

Figure 18: Path-generating inverter problem. Output displacement paths obtained with pixel-based (left) and body-fitted (right) meshes, for the proportional set of control points and $\sigma_y = 0.05$.

the final deformed configuration, in which the stress constraints are applied. Both the pixel-based and body-fitted schemes are applied to obtain the $\eta \times \sigma_{max}$ graphs; these are shown in Figure 21. The pixel-based graphs (solid lines) are obtained for incremental steps of 0.005, and the body-fitted graphs (points) are obtained for incremental steps of 0.025, for $\eta \in [\eta_d, \eta_e]$.

In these cases, we have maximum stress constraint violations of: 0.42% (fitted), for the proportional set of control points; and 0.35% (pixel), for the non-proportional set of control points. There were no stress constraint violations for the proportional set of control points with the pixel-based scheme and for the non-proportional set of control points

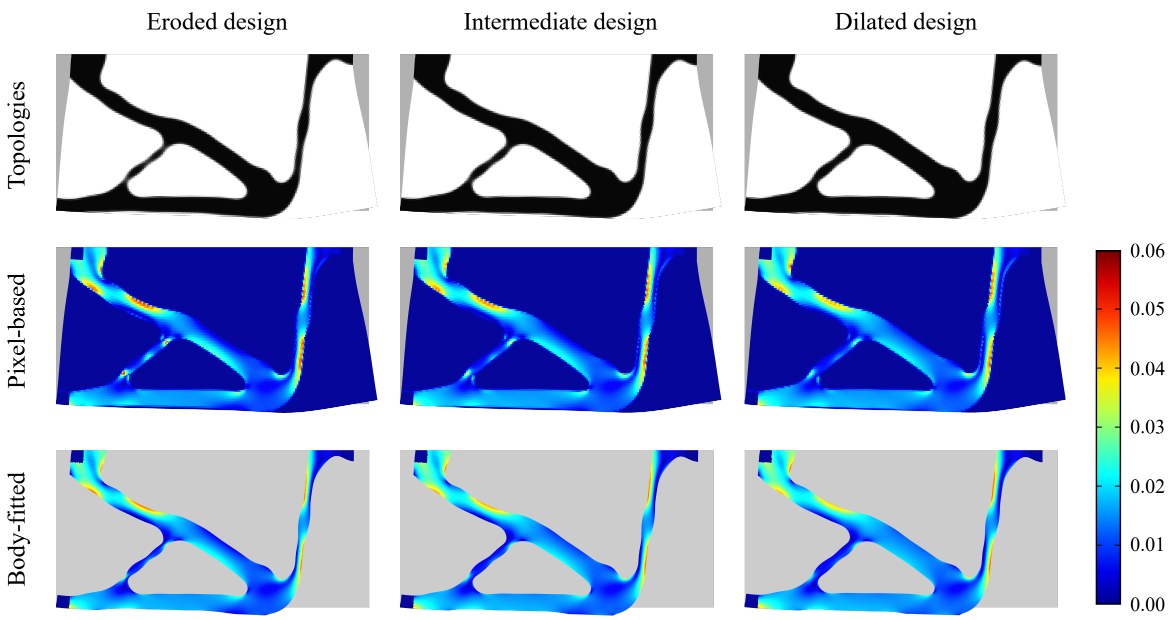

Figure 19: Path-generating inverter problem. Topologies, pixel-based and body-fitted von Mises stresses in deformed configuration, for the non-proportional set of control points and $\sigma_y = 0.05$.

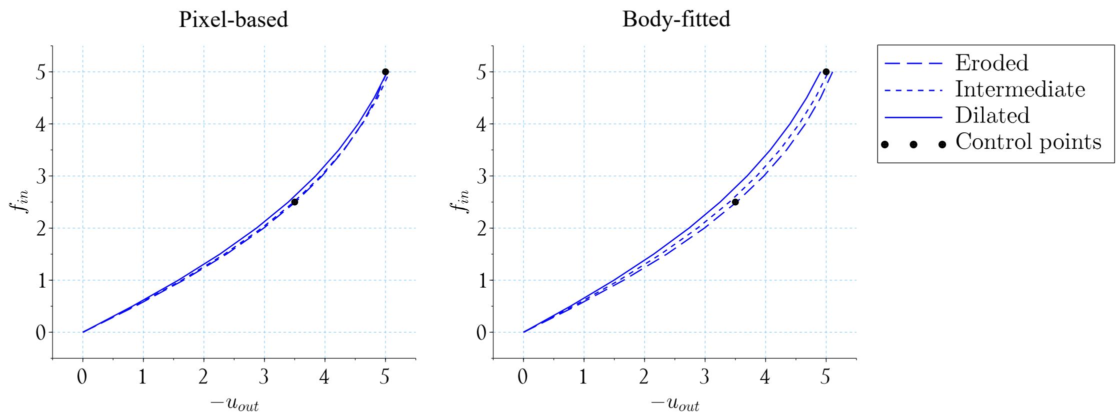

Figure 20: Path-generating inverter problem. Output displacement paths obtained with pixel-based (left) and body-fitted (right) meshes, for the non-proportional set of control points and $\sigma_y = 0.05$.

with the body-fitted scheme.

7. Concluding remarks

This work has proposed and investigated two formulations to topology design of compliant mechanisms considering stress constraints, manufacturing uncertainty and geometric nonlinearity. The first approach is an extension of the stress-constrained maximum output displacement formulation, and the second approach is an extension of the standard path-generating design formulation. Several numerical examples were solved to demonstrate the applicability

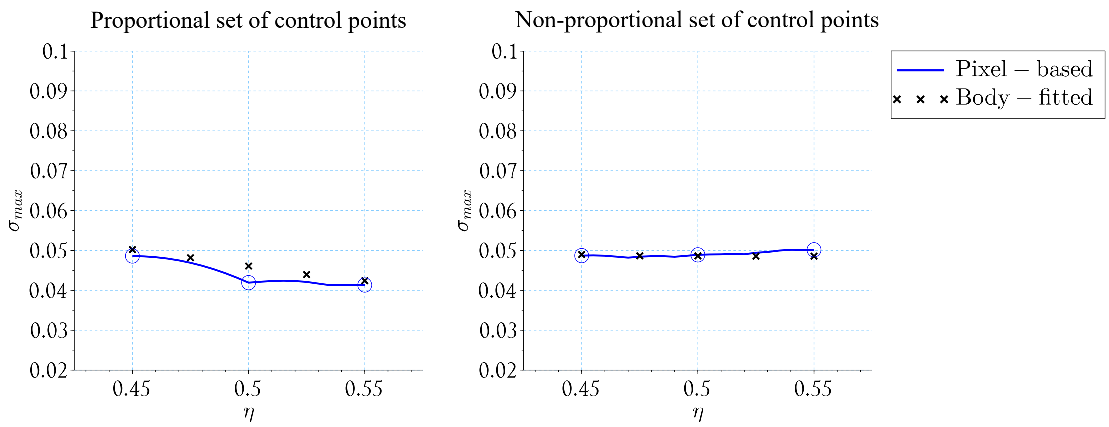

Figure 21: Maximum von Mises stresses for different values of η (uniform boundary variation), for the results from Figures 17 (left) and 19 (right).

of the proposed approaches. The numerical results were post-processed with use of pixel-based and body-fitted post-processing schemes. Main conclusions are:

1. The proposed maximum output displacement formulation was able to provide optimized structures with maximum von Mises stresses almost insensitive to uniform boundary variation. The proposed stress interpolation scheme, to be used together with the energy interpolation scheme, worked fine in all cases, since good agreements between pixel-based and body-fitted von Mises stresses were obtained. Moreover, small stress constraint violations were observed in all cases where the stress constraint was applied.
2. Numerical comparisons between nonlinear and linear analyses in the maximum output displacement formulation demonstrated the importance of using nonlinear analysis during the optimization process. Although small differences in shape were observed, structures obtained with the maximum output displacement formulation together with the linear analysis demonstrated instability, with rapidly varying maximum von Mises stresses and large stress constraint violations after uniform boundary variation. Moreover, it was demonstrated that the topologies obtained with the nonlinear formulation outperform the topologies obtained with linear analysis in both stress requirement and output performance of the compliant mechanism.
3. The proposed path-generating formulation was able to provide optimized structures with different equilibrium paths. Numerical examples demonstrated the importance of using the double filter approach in this case, to provide almost black and white solutions, where the intermediate material is only present at the smooth transition boundaries between solid and void phases.
4. An almost perfect fit was observed between computed and prescribed control points in the path-generating design problems. A slight deviation from the prescribed path was observed for very strong stress requirements, suggesting strong stress requirements and path-generating to be incompatible. Good fits were also observed

between the prescribed control points and the displacement paths obtained with the body-fitted finite element meshes.

Acknowledgements

G. A. da Silva would like to thank Prof. Humberto Breves Coda, from the University of São Paulo, for valuable discussion on finite strain theory. A. T. Beck and G. A. da Silva kindly acknowledge financial support of this research project by the agencies CNPq (National Council for Research and Development), grant number 306373/2016-5, and FAPESP (São Paulo Research Foundation), grant numbers 2018/16701-1 and 2019/08654-6. This study was financed in part by the Coordination for the Improvement of Higher Education Personnel - Brazil (CAPES) - Finance Code 001. O. Sigmund was supported by the Villum Investigator Project InnoTop funded by the Villum Foundation.

Appendix: Sensitivity analysis

This section develops the derivative of the augmented Lagrangian function, L, with respect to a design variable, ρ_m, necessary to use a gradient-based algorithm in the optimization process.

Maximum output displacement problem

The augmented Lagrangian function for the maximum output displacement problem, Equation (32), can be properly rewritten in order to facilitate sensitivity analysis by the adjoint technique:

$$L = L_V + L_{u\sigma}, \tag{.1}$$

where L_V is the term associated with the volume fraction of the dilated design

$$L_V = k_v V_f\left(\overline{\boldsymbol{\rho}}^{(d)}\right) + \frac{r_{up}}{2}\left\langle \frac{\mu_{up}}{r_{up}} + \frac{V_f\left(\overline{\boldsymbol{\rho}}^{(d)}\right)}{V_{up}^{(d)}} - 1 \right\rangle^2 + \frac{r_{low}}{2}\left\langle \frac{\mu_{low}}{r_{low}} - \frac{V_f\left(\overline{\boldsymbol{\rho}}^{(d)}\right)}{V_{low}^{(d)}} + 1 \right\rangle^2, \tag{.2}$$

and $L_{u\sigma}$ is the term associated with both the output displacements and stress constraints

$$L_{u\sigma} = \frac{k_{in}}{f_{in}} u_{out}^{KS}\left(\overline{\boldsymbol{\rho}}^{(e)}, \overline{\boldsymbol{\rho}}^{(i)}, \overline{\boldsymbol{\rho}}^{(d)}\right) + \frac{r}{2}\sum_{k=1}^{N_k}\sum_{j\in S}\left\langle \frac{\mu_k^{(j)}}{r} + \frac{\sigma_{eq}^{(k)}\left(\overline{\boldsymbol{\rho}}^{(j)}\right)}{\sigma_y} - 1 \right\rangle^2 + \sum_{j\in S}\boldsymbol{\lambda}_{(j)}^T \mathbf{R}\left(\mathbf{Y}\left(\overline{\boldsymbol{\rho}}^{(j)}\right)\right), \tag{.3}$$

where $S = \{e, i, d\}$ is the set which contains dilated, intermediate and eroded fields of physical relative densities, and $\boldsymbol{\lambda}_{(j)}$ are arbitrary vectors, since $\mathbf{R}\left(\mathbf{Y}\left(\overline{\boldsymbol{\rho}}^{(j)}\right)\right) = \mathbf{0}$.

The derivative of the augmented Lagrangian function can be computed through a chain rule [51]

$$\frac{\partial L}{\partial \rho_m} = \sum_{n\in\vartheta_m} \frac{\partial L_V}{\partial \overline{\rho}_n^{(d)}} \frac{\partial \overline{\rho}_n^{(d)}}{\partial \tilde{\rho}_n} \frac{\partial \tilde{\rho}_n}{\partial \rho_m} + \sum_{j\in S} \sum_{n\in\vartheta_m} \frac{\partial L_{u\sigma}}{\partial \overline{\rho}_n^{(j)}} \frac{\partial \overline{\rho}_n^{(j)}}{\partial \tilde{\rho}_n} \frac{\partial \tilde{\rho}_n}{\partial \rho_m}, \tag{.4}$$

where

$$\frac{\partial L_V}{\partial \overline{\rho}_n^{(d)}} = \frac{V_n}{V_{domain}} \left[k_v + \left\langle \mu_{up} + r_{up} \left(\frac{V_f\left(\overline{\boldsymbol{\rho}}^{(d)}\right)}{V_{up}^{(d)}} - 1 \right) \right\rangle \frac{1}{V_{up}^{(d)}} - \left\langle \mu_{low} + r_{low} \left(-\frac{V_f\left(\overline{\boldsymbol{\rho}}^{(d)}\right)}{V_{low}^{(d)}} + 1 \right) \right\rangle \frac{1}{V_{low}^{(d)}} \right] \tag{.5}$$

is the derivative of Equation (.2),

$$\frac{\partial \overline{\rho}_n^{(j)}}{\partial \tilde{\rho}_n} = \frac{\beta(\mathrm{sech}(\beta(\tilde{\rho}_n - \eta_j)))^2}{\tanh(\beta\eta_j) + \tanh(\beta(1-\eta_j))} \tag{.6}$$

is the derivative of Equation (2), and

$$\frac{\partial \tilde{\rho}_n}{\partial \rho_m} = \frac{w(\mathbf{x}_m)V_m}{\sum_{o\in\vartheta_n} w(\mathbf{x}_o)V_o} \tag{.7}$$

is the derivative of Equation (3).

The derivative of $L_{u\sigma}$, Equation (.3), with respect to $\overline{\rho}_n^{(j)}$ is given by

$$\frac{\partial L_{u\sigma}}{\partial \overline{\rho}_n^{(j)}} = \frac{k_{in}}{f_{in}} \frac{\exp\left(P\, u_{out}\left(\overline{\boldsymbol{\rho}}^{(j)}\right)\right)}{\exp\left(P\, u_{out}^{KS}\right)} \frac{\partial u_{out}\left(\overline{\boldsymbol{\rho}}^{(j)}\right)}{\partial \overline{\rho}_n^{(j)}} + \sum_{k=1}^{N_k} h_k^{(j)} \frac{\partial \sigma_{eq}^{(k)}\left(\overline{\boldsymbol{\rho}}^{(j)}\right)}{\partial \overline{\rho}_n^{(j)}} + \boldsymbol{\lambda}_{(j)}^T \left[\frac{\partial \mathbf{R}\left(\mathbf{Y}\left(\overline{\boldsymbol{\rho}}^{(j)}\right)\right)}{\partial \mathbf{Y}\left(\overline{\boldsymbol{\rho}}^{(j)}\right)} \frac{\partial \mathbf{Y}\left(\overline{\boldsymbol{\rho}}^{(j)}\right)}{\partial \overline{\rho}_n^{(j)}} + \frac{\partial \mathbf{F}_{int}\left(\mathbf{Y}\left(\overline{\boldsymbol{\rho}}^{(j)}\right)\right)}{\partial \overline{\rho}_n^{(j)}} \right], \tag{.8}$$

where

$$h_k^{(j)} = \left\langle \mu_k^{(j)} + r \left(\frac{\sigma_{eq}^{(k)}\left(\overline{\boldsymbol{\rho}}^{(j)}\right)}{\sigma_y} - 1 \right) \right\rangle \frac{1}{\sigma_y}. \tag{.9}$$

From now on, we will drop the dependence of the notation on $\overline{\boldsymbol{\rho}}^{(j)}$ for a clearer mathematical development. The derivative of the von Mises equivalent stress at point k, Equation (5), is given by

$$\frac{\partial \sigma_{eq}^{(k)}}{\partial \overline{\rho}_n^{(j)}} = \frac{\partial f_\sigma}{\partial \overline{\rho}_n^{(j)}} \hat{\sigma}_{eq}^{(k)} + f_\sigma \frac{\partial \hat{\sigma}_{eq}^{(k)}}{\partial \overline{\rho}_n^{(j)}}, \tag{.10}$$

where the derivative of the solid von Mises stress, $\hat{\sigma}_{eq}^{(k)}$, is given by

$$\frac{\partial \hat{\sigma}_{eq}^{(k)}}{\partial \overline{\rho}_n^{(j)}} = \frac{1}{\hat{\sigma}_{eq}^{(k)}} \left[\left(\hat{\sigma}_{11(k)} - \frac{\hat{\sigma}_{22(k)}}{2} \right) \frac{\partial \hat{\sigma}_{11(k)}}{\partial \overline{\rho}_n^{(j)}} + \left(\hat{\sigma}_{22(k)} - \frac{\hat{\sigma}_{11(k)}}{2} \right) \frac{\partial \hat{\sigma}_{22(k)}}{\partial \overline{\rho}_n^{(j)}} + 3\hat{\sigma}_{12(k)} \frac{\partial \hat{\sigma}_{12(k)}}{\partial \overline{\rho}_n^{(j)}} \right]. \tag{.11}$$

The derivatives of the Cauchy stress components, $\frac{\partial \hat{\sigma}_{11(k)}}{\partial \overline{\rho}_n^{(j)}}$, $\frac{\partial \hat{\sigma}_{22(k)}}{\partial \overline{\rho}_n^{(j)}}$ and $\frac{\partial \hat{\sigma}_{12(k)}}{\partial \overline{\rho}_n^{(j)}}$, necessary to compute the derivative of the solid von Mises stress, Equation (.11), are obtained through the derivative of the solid Cauchy stress tensor, Equation

(29), as follows

$$\frac{\partial \hat{\boldsymbol{\sigma}}_{(k)}}{\partial \overline{\rho}_n^{(j)}} = \gamma_k \sum_{a=1}^{n_{dof}} \frac{\partial \hat{\boldsymbol{\sigma}}_{(k)}^{NL}}{\partial y_a^{(k)}} \frac{\partial y_a^{(k)}}{\partial \overline{\rho}_n^{(j)}} + \frac{\partial \gamma_k}{\partial \overline{\rho}_n^{(j)}} \hat{\boldsymbol{\sigma}}_{(k)}^{NL} + (1-\gamma_k) \sum_{a=1}^{n_{dof}} \frac{\partial \hat{\boldsymbol{\sigma}}_{(k)}^{L}}{\partial y_a^{(k)}} \frac{\partial y_a^{(k)}}{\partial \overline{\rho}_n^{(j)}} - \frac{\partial \gamma_k}{\partial \overline{\rho}_n^{(j)}} \hat{\boldsymbol{\sigma}}_{(k)}^{L} \tag{.12}$$

where n_{dof} is the number of degrees of freedom of the element which contains point k.

The derivative of the solid stress considering the nonlinear material model and finite strain theory is given by the derivative of Equation (15), as follows

$$\begin{aligned}\frac{\partial \hat{\boldsymbol{\sigma}}_{(k)}^{NL}}{\partial y_a^{(k)}} = &- \frac{2\mu\, J_{(k)}}{\overline{J}_{(k)}^2 (\lambda + 2\mu)} \mathbf{C}_{(k)}^{-1} : \frac{\partial \mathbf{E}_{(k)}}{\partial y_a^{(k)}} \mathbf{A}_{(k)} \mathbf{S}_{(k)}^{NL} \mathbf{A}_{(k)}^T + J_{(k)}^{-1} \frac{\partial \mathbf{A}_{(k)}}{\partial y_a^{(k)}} \mathbf{S}_{(k)}^{NL} \mathbf{A}_{(k)}^T \\ &+ J_{(k)}^{-1} \mathbf{A}_{(k)} \frac{\partial \mathbf{S}_{(k)}^{NL}}{\partial \mathbf{E}_{(k)}} : \frac{\partial \mathbf{E}_{(k)}}{\partial y_a^{(k)}} \mathbf{A}_{(k)}^T + J_{(k)}^{-1} \mathbf{A}_{(k)} \mathbf{S}_{(k)}^{NL} \frac{\partial \mathbf{A}_{(k)}^T}{\partial y_a^{(k)}},\end{aligned} \tag{.13}$$

whereas the derivative of the solid stress considering the linear material model and infinitesimal strain theory is given by the derivative of Equation (20), as follows

$$\frac{\partial \hat{\boldsymbol{\sigma}}_{(k)}^{L}}{\partial y_a^{(k)}} = \frac{\partial \hat{\boldsymbol{\sigma}}_{(k)}^{L}}{\partial \boldsymbol{\varepsilon}_{(k)}} : \frac{\partial \boldsymbol{\varepsilon}_{(k)}}{\partial y_a^{(k)}}. \tag{.14}$$

Equation (.12) is rewritten as

$$\frac{\partial \hat{\boldsymbol{\sigma}}_{(k)}}{\partial \overline{\rho}_n^{(j)}} = \left(\hat{\boldsymbol{\sigma}}_{(k)}^{NL} - \hat{\boldsymbol{\sigma}}_{(k)}^{L}\right) \frac{\partial \gamma_k}{\partial \overline{\rho}_n^{(j)}} + \sum_{a=1}^{n_{dof}} \left(\gamma_k \frac{\partial \hat{\boldsymbol{\sigma}}_{(k)}^{NL}}{\partial y_a^{(k)}} + (1-\gamma_k) \frac{\partial \hat{\boldsymbol{\sigma}}_{(k)}^{L}}{\partial y_a^{(k)}}\right) \frac{\partial y_a^{(k)}}{\partial \overline{\rho}_n^{(j)}}, \tag{.15}$$

and then, the corresponding stress components of this derivative are substituted in Equation (.11). After proper manipulation, Equation (.11) can be rewritten as

$$\frac{\partial \hat{\sigma}_{eq}^{(k)}}{\partial \overline{\rho}_n^{(j)}} = \frac{1}{\hat{\sigma}_{eq}^{(k)}} \sum_{a=1}^{n_{dof}} \mathcal{F}_a^{(k)} \frac{\partial y_a^{(k)}}{\partial \overline{\rho}_n^{(j)}} + \frac{1}{\hat{\sigma}_{eq}^{(k)}} \mathcal{P}^{(k)} \frac{\partial \gamma_k}{\partial \overline{\rho}_n^{(j)}}, \tag{.16}$$

where

$$\begin{aligned}\mathcal{F}_a^{(k)} = &\left(\hat{\sigma}_{11(k)} - \frac{\hat{\sigma}_{22(k)}}{2}\right)\left(\gamma_k \frac{\partial \hat{\sigma}_{11(k)}^{NL}}{\partial y_a^{(k)}} + (1-\gamma_k) \frac{\partial \hat{\sigma}_{11(k)}^{L}}{\partial y_a^{(k)}}\right) + \left(\hat{\sigma}_{22(k)} - \frac{\hat{\sigma}_{11(k)}}{2}\right)\left(\gamma_k \frac{\partial \hat{\sigma}_{22(k)}^{NL}}{\partial y_a^{(k)}} + (1-\gamma_k) \frac{\partial \hat{\sigma}_{22(k)}^{L}}{\partial y_a^{(k)}}\right) \\ &+ 3\hat{\sigma}_{12(k)} \left(\gamma_k \frac{\partial \hat{\sigma}_{12(k)}^{NL}}{\partial y_a^{(k)}} + (1-\gamma_k) \frac{\partial \hat{\sigma}_{12(k)}^{L}}{\partial y_a^{(k)}}\right),\end{aligned} \tag{.17}$$

and

$$\mathcal{P}^{(k)} = \left(\hat{\sigma}_{11(k)} - \frac{\hat{\sigma}_{22(k)}}{2}\right)\left(\hat{\sigma}_{11(k)}^{NL} - \hat{\sigma}_{11(k)}^{L}\right) + \left(\hat{\sigma}_{22(k)} - \frac{\hat{\sigma}_{11(k)}}{2}\right)\left(\hat{\sigma}_{22(k)}^{NL} - \hat{\sigma}_{22(k)}^{L}\right) + 3\hat{\sigma}_{12(k)}\left(\hat{\sigma}_{12(k)}^{NL} - \hat{\sigma}_{12(k)}^{L}\right). \tag{.18}$$

Substituting Equation (.16) in Equation (.10), gives

$$\frac{\partial \sigma_{eq}^{(k)}}{\partial \overline{\rho}_n^{(j)}} = \frac{\partial f_\sigma}{\partial \overline{\rho}_n^{(j)}} \hat{\sigma}_{eq}^{(k)} + \frac{f_\sigma}{\hat{\sigma}_{eq}^{(k)}} \sum_{a=1}^{n_{dof}} \mathcal{F}_a^{(k)} \frac{\partial y_a^{(k)}}{\partial \overline{\rho}_n^{(j)}} + \frac{f_\sigma}{\hat{\sigma}_{eq}^{(k)}} \mathcal{P}^{(k)} \frac{\partial \gamma_k}{\partial \overline{\rho}_n^{(j)}}, \tag{.19}$$

which is then substituted in Equation (.8), resulting in the following equation

$$\begin{aligned}\frac{\partial L_{u\sigma}}{\partial \overline{\rho}_n^{(j)}} =& \frac{k_{in}}{f_{in}} \frac{\exp\left(P\, u_{out}\right)}{\exp\left(P\, u_{out}^{KS}\right)} \boldsymbol{\Lambda}_{out}^T \frac{\partial \mathbf{U}}{\partial \overline{\rho}_n^{(j)}} + \sum_{k=1}^{N_k} h_k^{(j)} \left(\frac{\partial f_\sigma}{\partial \overline{\rho}_n^{(j)}} \hat{\sigma}_{eq}^{(k)} + \frac{f_\sigma}{\hat{\sigma}_{eq}^{(k)}} \mathcal{P}^{(k)} \frac{\partial \gamma_k}{\partial \overline{\rho}_n^{(j)}} \right) \\ &+ \sum_{k=1}^{N_k} h_k^{(j)} \frac{f_\sigma}{\hat{\sigma}_{eq}^{(k)}} \sum_{a=1}^{n_{dof}} \mathcal{F}_a^{(k)} \mathbf{H}_a^{(k)} \frac{\partial \mathbf{Y}}{\partial \overline{\rho}_n^{(j)}} + \boldsymbol{\lambda}_{(j)}^T \frac{\partial \mathbf{R}\left(\mathbf{Y}\right)}{\partial \mathbf{Y}} \frac{\partial \mathbf{Y}}{\partial \overline{\rho}_n^{(j)}} + \boldsymbol{\lambda}_{(j)}^T \frac{\partial \mathbf{F}_{int}\left(\mathbf{Y}\right)}{\partial \overline{\rho}_n^{(j)}},\end{aligned} \tag{.20}$$

where the localization operator $\mathbf{H}_a^{(k)} \mathbf{Y} = y_a^{(k)}$ is used. Exploiting the fact that $\frac{\partial \mathbf{U}}{\partial \overline{\rho}_n^{(j)}} = \frac{\partial \mathbf{Y}}{\partial \overline{\rho}_n^{(j)}}$, Equation (.20) is rewritten as

$$\begin{aligned}\frac{\partial L_{u\sigma}}{\partial \overline{\rho}_n^{(j)}} =& \sum_{k=1}^{N_k} h_k^{(j)} \left(\frac{\partial f_\sigma}{\partial \overline{\rho}_n^{(j)}} \hat{\sigma}_{eq}^{(k)} + \frac{f_\sigma}{\hat{\sigma}_{eq}^{(k)}} \mathcal{P}^{(k)} \frac{\partial \gamma_k}{\partial \overline{\rho}_n^{(j)}} \right) + \boldsymbol{\lambda}_{(j)}^T \frac{\partial \mathbf{F}_{int}\left(\mathbf{Y}\right)}{\partial \overline{\rho}_n^{(j)}} \\ &+ \left(\frac{k_{in}}{f_{in}} \frac{\exp\left(P\, u_{out}\right)}{\exp\left(P\, u_{out}^{KS}\right)} \boldsymbol{\Lambda}_{out}^T + \sum_{k=1}^{N_k} h_k^{(j)} \frac{f_\sigma}{\hat{\sigma}_{eq}^{(k)}} \sum_{a=1}^{n_{dof}} \mathcal{F}_a^{(k)} \mathbf{H}_a^{(k)} \frac{\partial \mathbf{Y}}{\partial \overline{\rho}_n^{(j)}} + \boldsymbol{\lambda}_{(j)}^T \frac{\partial \mathbf{R}\left(\mathbf{Y}\right)}{\partial \mathbf{Y}} \right) \frac{\partial \mathbf{Y}}{\partial \overline{\rho}_n^{(j)}}.\end{aligned} \tag{.21}$$

In order to avoid the computation of $\frac{\partial \mathbf{Y}}{\partial \overline{\rho}_n^{(j)}}$, the adjoint vector is computed as

$$\frac{\partial \mathbf{R}\left(\mathbf{Y}\right)}{\partial \mathbf{Y}} \boldsymbol{\lambda}_{(j)} = -\frac{k_{in}}{f_{in}} \frac{\exp\left(P\, u_{out}\right)}{\exp\left(P\, u_{out}^{KS}\right)} \boldsymbol{\Lambda}_{out} - \sum_{k=1}^{N_k} h_k^{(j)} \frac{f_\sigma}{\hat{\sigma}_{eq}^{(k)}} \sum_{a=1}^{n_{dof}} \mathcal{F}_a^{(k)} \left(\mathbf{H}_a^{(k)}\right)^T. \tag{.22}$$

After computing the adjoint vector $\boldsymbol{\lambda}_{(j)}$, Equation (.22), the derivative of $L_{u\sigma}$ with respect to $\overline{\rho}_n^{(j)}$, given by Equation (.21), is then obtained through local computations, as follows

$$\frac{\partial L_{u\sigma}}{\partial \overline{\rho}_n^{(j)}} = h_n^{(j)} \left(\frac{\partial f_\sigma}{\partial \overline{\rho}_n^{(j)}} \hat{\sigma}_{eq}^{(n)} + \frac{f_\sigma}{\hat{\sigma}_{eq}^{(n)}} \mathcal{P}^{(n)} \frac{\partial \gamma_n}{\partial \overline{\rho}_n^{(j)}} \right) + \boldsymbol{\lambda}_{(j,n)}^T \frac{\partial \mathbf{f}_{int}^{(n)}\left(\mathbf{y}_n\right)}{\partial \overline{\rho}_n^{(j)}}, \tag{.23}$$

where $\boldsymbol{\lambda}_{(j,n)}$ is the local adjoint vector associated with element n, and $\frac{\partial \mathbf{f}_{int}^{(n)}(\mathbf{y}_n)}{\partial \overline{\rho}_n^{(j)}}$ is the derivative of the local internal force vector associated with element n.

The derivative of the augmented Lagrangian function, L, with respect to a design variable, ρ_m, is then computed by substituting Equations (.5), (.6), (.7) and (.23) in Equation (.4). Note that, as in the linear case [35], three adjoint problems, Equation (.22), need to be solved per iteration, one for each relative density field, in order to evaluate the gradient of the augmented Lagrangian function.

Path-generating problem

The derivative of the augmented Lagrangian function associated with the path-generating formulation, Equation (33), is developed by employing the step-by-step procedure presented for the maximum output displacement case, with straightforward modifications; thus, it is not presented herein. We just show how the augmented Lagrangian may be written to facilitate use of the adjoint method in this case, and the final adjoint problems. The augmented Lagrangian is written as:

$$L = L_V + L_{u\sigma,M} + \sum_{m=1}^{M-1} L_{u,m}, \tag{.24}$$

where L_V is the term associated with the volume fraction of the dilated design

$$L_V = \frac{r_{up}}{2} \left\langle \frac{\mu_{up}}{r_{up}} + \frac{V_f\left(\overline{\overline{\boldsymbol{\rho}}}^{(d)}\right)}{V_{up}^{(d)}} - 1 \right\rangle^2, \tag{.25}$$

$L_{u\sigma,M}$ is the term associated with both the final control point and the stress constraints

$$L_{u\sigma,M} = \left(\frac{k_{in}}{f_{in,M}}\right)^2 \sum_{j\in S} \left(u_{out,M}\left(\overline{\overline{\boldsymbol{\rho}}}^{(j)}\right) - u^*_{out,M}\right)^2 + \frac{r}{2} \sum_{k=1}^{N_k} \sum_{j\in S} \left\langle \frac{\mu_k^{(j)}}{r} + \frac{\sigma_{eq}^{(k)}\left(\overline{\overline{\boldsymbol{\rho}}}^{(j)}\right)}{\sigma_y} - 1 \right\rangle^2 + \sum_{j\in S} \boldsymbol{\lambda}_{(j),M}^T \mathbf{R}\left(\mathbf{Y}_M\left(\overline{\overline{\boldsymbol{\rho}}}^{(j)}\right)\right), \tag{.26}$$

and $L_{u,m}$ is the term associated with the m-th control point

$$L_{u,m} = \left(\frac{k_{in}}{f_{in,M}}\right)^2 \sum_{j\in S} \left(u_{out,m}\left(\overline{\overline{\boldsymbol{\rho}}}^{(j)}\right) - u^*_{out,m}\right)^2 + \sum_{j\in S} \boldsymbol{\lambda}_{(j),m}^T \mathbf{R}\left(\mathbf{Y}_m\left(\overline{\overline{\boldsymbol{\rho}}}^{(j)}\right)\right). \tag{.27}$$

The adjoint problems are given by

$$\frac{\partial \mathbf{R}\left(\mathbf{Y}_M\right)}{\partial \mathbf{Y}_M} \boldsymbol{\lambda}_{(j),M} = -2\left(\frac{k_{in}}{f_{in,M}}\right)^2 \left(u_{out,M} - u^*_{out,M}\right) \boldsymbol{\Lambda}_{out} - \sum_{k=1}^{N_k} h_k^{(j)} \frac{f_\sigma}{\hat{\sigma}_{eq}^{(k)}} \sum_{a=1}^{n_{dof}} \mathcal{F}_a^{(k)} \left(\mathbf{H}_a^{(k)}\right)^T, \tag{.28}$$

and

$$\frac{\partial \mathbf{R}\left(\mathbf{Y}_m\right)}{\partial \mathbf{Y}_m} \boldsymbol{\lambda}_{(j),m} = -2\left(\frac{k_{in}}{f_{in,M}}\right)^2 \left(u_{out,m} - u^*_{out,m}\right) \boldsymbol{\Lambda}_{out}. \tag{.29}$$

Note that Equations (.28) and (.22) are quite similar. The differences are in the terms associated with output displacement. The term associated with the stress constraints is the same, though.

After computing the adjoint vectors, the derivative of $L_{u\sigma,M}$ with respect to a physical variable $\overline{\overline{\rho}}_n^{(j)}$ is given by Equation (.23), whereas the derivative of $L_{u,m}$ is given by the same equation disregarding the term associated with the stress constraints.

Since the double filter approach is employed in this case, the chain rule from [45] should be employed, instead of Equation (.4), to obtain the final derivatives. Note that, in the path-generating problem, $3M$ adjoint problems need to be solved per iteration (three for each prescribed control point).

References

[1] M. P. Bendsøe, O. Sigmund, Topology Optimization: Theory, Methods and Applications, Springer, Berlin, 2003 (2003). doi:10.1007/978-3-662-05086-6.

[2] O. Sigmund, K. Maute, Topology optimization approaches, Structural and Multidisciplinary Optimization 48 (6) (2013) 1031 – 1055 (2013). doi:10.1007/s00158-013-0978-6.

[3] O. Sigmund, On the design of compliant mechanisms using topology optimization, Mechanics of Structures and Machines 25 (4) (1997) 493 – 524 (1997). doi:10.1080/08905459708945415.

[4] F. Wang, B. S. Lazarov, O. Sigmund, J. S. Jensen, Interpolation scheme for fictitious domain techniques and topology optimization of finite strain elastic problems, Computer Methods in Applied Mechanics and Engineering 276 (2014) 453 – 472 (2014). doi:doi.org/10.1016/j.cma.2014.03.021.

[5] T. Buhl, C. Pedersen, O. Sigmund, Stiffness design of geometrically nonlinear structures using topology optimization, Structural and Multidisciplinary Optimization 19 (2) (2000) 93–104 (2000). doi:10.1007/s001580050089.

[6] C. B. W. Pedersen, T. Buhl, O. Sigmund, Topology synthesis of large-displacement compliant mechanisms, International Journal for Numerical Methods in Engineering 50 (12) (2001) 2683–2705 (2001). doi:10.1002/nme.148.

[7] T. E. Bruns, D. A. Tortorelli, An element removal and reintroduction strategy for the topology optimization of structures and compliant mechanisms, International Journal for Numerical Methods in Engineering 57 (10) (2003) 1413–1430 (2003). doi:10.1002/nme.783.

[8] G. H. Yoon, Y. Y. Kim, Element connectivity parameterization for topology optimization of geometrically nonlinear structures, International Journal of Solids and Structures 42 (7) (2005) 1983 – 2009 (2005). doi:10.1016/j.ijsolstr.2004.09.005.

[9] A. Klarbring, N. Strömberg, Topology optimization of hyperelastic bodies including non-zero prescribed displacements, Structural and Multidisciplinary Optimization 47 (1) (2013) 37–48 (2013). doi:10.1007/s00158-012-0819-z.

[10] S. J. Moon, G. H. Yoon, A newly developed qp-relaxation method for element connectivity parameterization to achieve stress-based topology optimization for geometrically nonlinear structures, Computer Methods in Applied Mechanics and Engineering 265 (2013) 226 – 241 (2013). doi:10.1016/j.cma.2013.07.001.

[11] Y. Luo, M. Y. Wang, Z. Kang, Topology optimization of geometrically nonlinear structures based on an additive hyperelasticity technique, Computer Methods in Applied Mechanics and Engineering 286 (2015) 422 – 441 (2015). doi:10.1016/j.cma.2014.12.023.

[12] M. Wallin, N. Ivarsson, D. Tortorelli, Stiffness optimization of non-linear elastic structures, Computer Methods in Applied Mechanics and Engineering 330 (2018) 292 – 307 (2018). doi:10.1016/j.cma.2017.11.004.

[13] Y. Li, J. Zhu, F. Wang, W. Zhang, O. Sigmund, Shape preserving design of geometrically nonlinear structures using topology optimization, Structural and Multidisciplinary Optimization 59 (4) (2019) 1033–1051 (2019). doi:10.1007/s00158-018-2186-x.

[14] R. D. Lahuerta, E. T. Simões, E. M. B. Campello, P. M. Pimenta, E. C. N. Silva, Towards the stabilization of the low density elements in topology optimization with large deformation, Computational Mechanics 52 (4) (2013) 779–797 (2013). doi:10.1007/s00466-013-0843-x.

[15] P. Duysinx, M. P. Bendsøe, Topology optimization of continuum structures with local stress constraints, International Journal for Numerical Methods in Engineering 43 (8) (1998) 1453 – 1478 (1998). doi:10.1002/(SICI)1097-0207(19981230)43:8¡1453::AID-NME480¿3.0.CO;2-2.

[16] J. T. Pereira, E. A. Fancello, C. S. Barcellos, Topology optimization of continuum structures with material failure constraints, Structural and Multidisciplinary Optimization 26 (1-2) (2004) 50 – 66 (2004). doi:10.1007/s00158-003-0301-z.

[17] C. Le, J. Norato, T. Bruns, C. Ha, D. Tortorelli, Stress-based topology optimization for continua, Structural and Multidisciplinary Optimization 41 (4) (2010) 605 – 620 (2010). doi:10.1007/s00158-009-0440-y.

[18] S. Amstutz, A. A. Novotny, Topological optimization of structures subject to von mises stress constraints, Structural and Multidisciplinary Optimization 41 (3) (2010) 407 – 420 (2010). doi:10.1007/s00158-009-0425-x.

[19] X. Guo, W. S. Zhang, M. Y. Wang, P. Wei, Stress-related topology optimization via level set approach, Computer Methods in Applied Mechanics and Engineering 200 (47) (2011) 3439 – 3452 (2011). doi:10.1016/j.cma.2011.08.016.

[20] M. Bruggi, P. Duysinx, Topology optimization for minimum weight with compliance and stress constraints, Structural and Multidisciplinary Optimization 46 (3) (2012) 369–384 (2012). doi:10.1007/s00158-012-0759-7.

[21] E. Holmberg, B. Torstenfelt, A. Klarbring, Stress constrained topology optimization, Structural and Multidisciplinary Optimization 48 (1) (2013) 33–47 (2013). doi:10.1007/s00158-012-0880-7.

[22] H. Emmendoerfer, E. A. Fancello, A level set approach for topology optimization with local stress constraints, International Journal for Numerical Methods in Engineering 99 (2) (2014) 129 – 156 (2014). doi:10.1002/nme.4676.

[23] M. Collet, L. Noël, M. Bruggi, P. Duysinx, Topology optimization for microstructural design under stress constraints, Structural and Multidisciplinary Optimization 58 (6) (2018) 2677–2695 (2018). doi:10.1007/s00158-018-2045-9.

[24] M. A. Salazar de Troya, D. A. Tortorelli, Adaptive mesh refinement in stress-constrained topology optimization, Structural and Multidisciplinary Optimization 58 (6) (2018) 2369–2386 (2018). doi:10.1007/s00158-018-2084-2.

[25] R. Picelli, S. Townsend, C. Brampton, J. Norato, H. Kim, Stress-based shape and topology optimization with the level set method, Computer Methods in Applied Mechanics and Engineering 329 (2018) 1 – 23 (2018). doi:https://doi.org/10.1016/j.cma.2017.09.001.

[26] D. M. De Leon, J. Alexandersen, J. S. O. Fonseca, O. Sigmund, Stress-constrained topology optimization for compliant mechanism design, Structural and Multidisciplinary Optimization 52 (5) (2015) 929 – 943 (2015). doi:10.1007/s00158-015-1279-z.

[27] C. G. Lopes, A. A. Novotny, Topology design of compliant mechanisms with stress constraints based on the topological derivative concept, Structural and Multidisciplinary Optimization 54 (4) (2016) 737 – 746 (2016). doi:10.1007/s00158-016-1436-z.

[28] S. Chu, L. Gao, M. Xiao, Z. Luo, H. Li, Stress-based multi-material topology optimization of compliant mechanisms, International Journal for Numerical Methods in Engineering 113 (7) (2018) 1021 – 1044 (2018). doi:10.1002/nme.5697.

[29] A. de Assis Pereira, E. L. Cardoso, On the influence of local and global stress constraint and filtering radius on the design of hinge-free compliant mechanisms, Structural and Multidisciplinary Optimization 58 (2) (2018) 641 – 655 (2018). doi:10.1007/s00158-018-1915-5.

[30] C. Conlan-Smith, K. A. James, A stress-based topology optimization method for heterogeneous structures, Structural and Multidisciplinary Optimization (2019). doi:10.1007/s00158-019-02207-9.

[31] G. D. Cheng, X. Guo, ε-relaxed approach in structural topology optimization, Structural Optimization 13 (4) (1997) 258 – 266 (1997). doi:10.1007/BF01197454.

[32] M. Bruggi, On an alternative approach to stress constraints relaxation in topology optimization, Structural and Multidisciplinary Optimization 36 (2) (2008) 125 – 141 (2008). doi:10.1007/s00158-007-0203-6.

[33] P. Duysinx, O. Sigmund, New developments in handling stress constraints in optimal material distribution, in: 7th AIAA/USAF/NASA/ISSMO Symposium on Multidisciplinary Analysis and Optimization, 1998, pp. 1501 – 1509 (1998). doi:10.2514/6.1998-4906.

[34] G. A. da Silva, A. T. Beck, O. Sigmund, Stress-constrained topology optimization considering uniform manufacturing uncertainties, Computer Methods in Applied Mechanics and Engineering 344 (2019) 512 – 537 (2019). doi:10.1016/j.cma.2018.10.020.

[35] G. A. da Silva, A. T. Beck, O. Sigmund, Topology optimization of compliant mechanisms with stress constraints and manufacturing error

robustness, Computer Methods in Applied Mechanics and Engineering 354 (2019) 397 – 421 (2019). doi:10.1016/j.cma.2019.05.046.

[36] O. Sigmund, Manufacturing tolerant topology optimization, Acta Mechanica Sinica 25 (2) (2009) 227–239 (Apr 2009). doi:10.1007/s10409-009-0240-z.

[37] F. Wang, B. S. Lazarov, O. Sigmund, On projection methods, convergence and robust formulations in topology optimization, Structural and Multidisciplinary Optimization 43 (6) (2011) 767–784 (2011). doi:10.1007/s00158-010-0602-y.

[38] S. Chen, W. Chen, A new level-set based approach to shape and topology optimization under geometric uncertainty, Structural and Multidisciplinary Optimization 44 (1) (2011) 1 – 18 (2011). doi:10.1007/s00158-011-0660-9.

[39] F. Wang, J. S. Jensen, O. Sigmund, Robust topology optimization of photonic crystal waveguides with tailored dispersion properties, Journal of the Optical Society of America B 28 (3) (2011) 387 – 397 (2011). doi:10.1364/JOSAB.28.000387.

[40] M. Schevenels, B. Lazarov, O. Sigmund, Robust topology optimization accounting for spatially varying manufacturing errors, Computer Methods in Applied Mechanics and Engineering 200 (49) (2011) 3613 – 3627 (2011). doi:10.1016/j.cma.2011.08.006.

[41] B. S. Lazarov, M. Schevenels, O. Sigmund, Robust design of large-displacement compliant mechanisms, Mechanical Sciences 2 (2) (2011) 175 – 182 (2011). doi:10.5194/ms-2-175-2011.

[42] B. S. Lazarov, M. Schevenels, O. Sigmund, Topology optimization with geometric uncertainties by perturbation techniques, International Journal for Numerical Methods in Engineering 90 (11) (2012) 1321 – 1336 (2012). doi:10.1002/nme.3361.

[43] B. S. Lazarov, M. Schevenels, O. Sigmund, Topology optimization considering material and geometric uncertainties using stochastic collocation methods, Structural and Multidisciplinary Optimization 46 (4) (2012) 597 – 612 (2012). doi:10.1007/s00158-012-0791-7.

[44] X. Guo, W. Zhang, L. Zhang, Robust structural topology optimization considering boundary uncertainties, Computer Methods in Applied Mechanics and Engineering 253 (2013) 356 – 368 (2013). doi:10.1016/j.cma.2012.09.005.

[45] R. E. Christiansen, B. S. Lazarov, J. S. Jensen, O. Sigmund, Creating geometrically robust designs for highly sensitive problems using topology optimization, Structural and Multidisciplinary Optimization 52 (4) (2015) 737–754 (2015). doi:10.1007/s00158-015-1265-5.

[46] M. Jansen, G. Lombaert, M. Schevenels, Robust topology optimization of structures with imperfect geometry based on geometric nonlinear analysis, Computer Methods in Applied Mechanics and Engineering 285 (2015) 452 – 467 (2015). doi:10.1016/j.cma.2014.11.028.

[47] W. Zhang, Z. Kang, Robust shape and topology optimization considering geometric uncertainties with stochastic level set perturbation, International Journal for Numerical Methods in Engineering 110 (1) (2017) 31 – 56 (2017). doi:10.1002/nme.5344.

[48] D. Ruiz, O. Sigmund, Optimal design of robust piezoelectric microgrippers undergoing large displacements, Structural and Multidisciplinary Optimization 57 (1) (2018) 71–82 (2018). doi:10.1007/s00158-017-1863-5.

[49] K.-J. Bathe, Finite Element Procedures, Prentice Hall, Upper Sadle River, New Jersey, 1996 (1996).

[50] M. P. Bendsøe, Optimal shape design as a material distribution problem, Structural optimization 1 (4) (1989) 193–202 (1989). doi:10.1007/BF01650949.

[51] O. Sigmund, Morphology-based black and white filters for topology optimization, Structural and Multidisciplinary Optimization 33 (4-5) (2007) 401 – 424 (2007). doi:10.1007/s00158-006-0087-x.

[52] P. G. Ciarlet, Mathematical Elasticity. Volume I: Three-Dimensional Elasticity, North-Holland Publishing Company, Amsterdam, 1988 (1988).

[53] J. C. Simo, T. J. R. Hughes, Computational Inelasticity, Springer-Verlag, New York, 1998 (1998). doi:10.1007/b98904.

[54] J. Bonet, R. D. Wood, Nonlinear Continuum Mechanics for Finite Element Analysis, 2nd Edition, Cambridge University Press, New York, 2008 (2008). doi:10.1017/CBO9780511755446.

[55] H. B. Coda, M. Greco, A simple fem formulation for large deflection 2d frame analysis based on position description, Computer Methods in Applied Mechanics and Engineering 193 (33) (2004) 3541 – 3557 (2004). doi:10.1016/j.cma.2004.01.005.

[56] H. B. Coda, R. R. Paccola, An alternative positional fem formulation for geometrically non-linear analysis of shells: Curved triangular

isoparametric elements, Computational Mechanics 40 (1) (2007) 185–200 (2007). doi:10.1007/s00466-006-0094-1.

[57] H. B. Coda, A solid-like fem for geometrically non-linear 3d frames, Computer Methods in Applied Mechanics and Engineering 198 (47) (2009) 3712 – 3722 (2009). doi:10.1016/j.cma.2009.08.001.

[58] E. A. Fancello, J. T. Pereira, Structural topology optimization considering material failure constraints and multiple load conditions, Latin American Journal of Solids and Structures 1 (1) (2003) 3 – 24 (2003).

[59] E. G. Birgin, J. M. Martínez, Practical Augmented Lagrangian Methods for Constrained Optimization, Society for Industrial and Applied Mathematics, Philadelphia, PA, 2014 (2014). doi:10.1137/1.9781611973365.

[60] G. Kreisselmeier, R. Steinhauser, Systematic control design by optimizing a vector performance index, IFAC Proceedings Volumes 12 (7) (1979) 113 – 117 (1979). doi:10.1016/S1474-6670(17)65584-8.

[61] N. Olhoff, Multicriterion structural optimization via bound formulation and mathematical programming, Structural optimization 1 (1) (1989) 11 – 17 (1989). doi:10.1007/BF01743805.

[62] G. A. da Silva, A. T. Beck, E. L. Cardoso, Topology optimization of continuum structures with stress constraints and uncertainties in loading, International Journal for Numerical Methods in Engineering 113 (1) (2018) 153 – 178 (2018). doi:10.1002/nme.5607.

[63] A. Clausen, E. Andreassen, On filter boundary conditions in topology optimization, Structural and Multidisciplinary Optimization 56 (5) (2017) 1147–1155 (2017). doi:10.1007/s00158-017-1709-1.

[64] C. Geuzaine, J.-F. Remacle, Gmsh: A 3-d finite element mesh generator with built-in pre- and post-processing facilities, International Journal for Numerical Methods in Engineering 79 (11) (2009) 1309–1331 (2009). doi:10.1002/nme.2579.